# Non-sulfide zinc deposits of the Moroccan High Atlas: Multi-scale characterization and origin

Flavien Choulet, Nicolas Charles, Luc Barbanson, Yannick Branquet, Stanislas Sizaret, Aomar Ennaciri, Lakhlifi Brada, Yan Chen

# Non-sulfide zinc deposits of the Moroccan High Atlas:

# Multi-scale characterization and origin

Flavien Choulet [1, *]; Nicolas Charles [2], Luc Barbanson [1], Yannick Branquet [1],Stanislas Sizaret [1], Aomar Ennaciri [3], Lakhlifi Badra [4], Yan Chen [1]

[1]: Institut des Sciences de la Terre d'Orléans, UMR 7327 - CNRS/Université d'Orléans/BRGM, Orléans, France

[2]: Bureau des Recherches Géologiques et Minières (BRGM), Orléans, France

[3]: Groupe Managem, Casablanca, Morocco

[4]: Université Moulay Ismaïl, Meknès, Morocco

[*]: flavien.choulet@univ-orleans.fr

Abstract

Six non-sulfide Zn-Pb ore deposits were investigated in the Moroccan High Atlas, to understand processes and timing of their formation. Sulfide and non-sulfide ores are hosted in Lower Jurassic reefal to para-reefal limestone. Zn (Pb) carbonates, Zn silicates and associated hydrated phases directly replace the stratabound primary ore bodies or fill cavities along fractures related to the Atlasic compression. Field observation has been complemented by a multidisciplinary approach (e.g. XRD, Raman, SEM, EPMA) for the mineralogical characterization. All six ore deposits present similar parageneses revealing three successive stages for ore deposition: 1) formation of the protore sulfides, 2) early supergene weathering

with formation of Zn-Pb-bearing carbonates and iron oxi-hydroxides and 3) late supergene weathering with deposition of Zn-carbonates, Zn-silicates and hydrated phases. Direct replacement of primary sulfides is accompanied by precipitation of zinc non-sulfide minerals in cavities or internal sediments filling. The proposed three-step scenario can be placed within the tectonic evolution of the Moroccan High Atlas belt. Deposition of primary sulfides is contemporaneous with opening of the Tethyan and Atlantic oceans. During the Tertiary, intracontinental deformation has given rise to the High Atlas fold-and-thrust belt and to regional uplift. As a result, Zn-Pb sulfides, hosted in carbonates experienced oxidation under an arid climate to form karst-related Zn-Pb non-sulfide ore bodies.

Keywords

Supergene deposits; non-sulfide Zn minerals; karst-related mineralization; in situ replacement of sulfides; Moroccan High Atlas

## 1) Introduction

Non-sulfide zinc ores, also called “calamines” or “zinc oxides” were the main sources of zinc metal using calcination until the end of the nineteenth century. This process was energy-intensive, whereas the development of mineral processing techniques, like flotation has contributed to effectively smelt sulfide raw materials. As a result, most of the zinc non-sulfide ores were abandoned (Hitzman et al., 2003), because flotation of zinc non-sulfide minerals was not selective enough (Bustamante and Shergold, 1983). However, recent improvement in hydrometallurgical acid-leaching, solvent extraction (SX) and electro-winning techniques (Cole and Sole 2002, Gnoinski, 2007; Hosseini, 2008) paves the way for a renewal of interest in non-sulfide ores.

Over the last decade, numerous supergene non-sulfide zinc deposits have been

reconsidered or discovered throughout the world (see reviews in Large, 2001; Boni and Large, 2003; Hitzman et al., 2003). Remarkable examples of such deposits are in Belgium (Dejonghe, 1998; Coppola et al., 2008), in Iran (Reichert et al., 2003; Daliran and Borg, 2009), in Sardinia (Boni et al., 2003), in Turkey (Santoro et al., 2013) and in southern Africa (Borg et al., 2003). Non-sulfide ore minerals usually include carbonates (smithsonite), hydrated carbonates (hydrozincite), silicates (willemite) and hydrated silicates (hemimorphite, Zn clays). Zinc is also incorporated in various complex phases (listed in Hitzman et al., 2003). The mineralogical characteristics help to separate the deposits into two major types: supergene and hypogene (Heyl and Bozion, 1962; Hitzman et al., 2003). The supergene type may be subdivided into three groups: direct-replacement deposits, wall-rock replacement deposits and karst-fill deposits (Hitzman et al., 2003). This nomenclature is somehow disputed (Borg, 2005), since several processes like direct replacement or wall rock replacement are usually involved in the formation of all supergene zinc ore deposits.

In supergene conditions, several features controlling the oxidation of primary sulfides and the development of supergene non-sulfide zinc deposits have been identified (Blanchard and Boswell, 1934; Smirnov, 1936; Reichert and Borg, 2008). The mineralogy of the primary ore body usually determines the paragenesis of the secondary ore deposits (Scott et al., 2001), although some elements like Zn and Cu can be very mobile under acidic conditions (Andrews-Jones, 1968). The geometry of the supergene non-sulfide zinc deposits is slightly influenced by the original morphology of the protore. The structure of the host rocks and the preexisting faults may facilitate the percolation of the meteoric waters and therefore represent the fundamental control of oxidizing solution flows (Borg, 2009). Oxidation process is limited and buffered by the nature of the host rocks (e.g. limestone host rocks) and its ability to interact with the generated acidic solution (Takahashi, 1960; Bladh, 1982; Sangameshwar and Barnes, 1983). Open or closed conditions of the karst system also influence the

equilibrium of solutions with atmosphere (Boni et al., 2003). The climatic factors (arid or wet conditions) control the amount of oxidizing meteoric water, the intensity of leaching and the possible reprecipitations (Reichert and Borg, 2008). Finally, the tectonic setting governs the regional uplift of the protore, in competition with erosion (Borg et al., 2003).

In Northern Africa, Zn-Pb ore deposits are numerous (Popov, 1968; Emberger, 1969 1970; Rouvier et al., 1985), and Zn ores of supergene origin have been long exploited for local and artisanal purpose using calcination to extract metals. Although several recent studies have refocused on supergene processes in Central and Northern Tunisia (Decrée et al., 2008; 2010; Bruyère et al., 2010), the supergene non-sulfide zinc deposits from other regions have been almost disregarded during the last three decades. In Morocco, the High Atlas Mountains contain a great number of non-sulfide Zn ore deposits (Emberger, 1969, 1970; Ovtracht, 1978), whose origin is not well constrained. Although the previous studies have established a genetic connection between the ore deposits, the karst network (Leblanc, 1968) and the folded and/or faulted structure of the Moroccan High Atlas (Bazin, 1968), the proposed genetic models (e.g. Ovtracht, 1978) are not consistent with the recent advances made on supergene non-sulfide zinc deposits throughout the world (e.g. Hitzman et al., 2003). Indeed, constraints on the mineralogy or the geometry of such deposits are often lacking and preclude a good understanding of their genesis.

In addition, the Moroccan High Atlas tectonics has been recently re-evaluated (e.g. Frizon de Lamotte et al., 2000; 2009). Those works highlight a complex evolution with several successive episodes of uplift related to intra-plate tectonics. The architecture of the belt is well constrained, either at surface (Teixell et al., 2003), or at great depth (Beauchamp et al., 1999; Arboleya et al., 2004). Arid conditions seem to have predominated during the last tens of millions of years (Maley, 1980; Le Houérou, 1997), although alternations of wet and arid conditions are recurrent (Rognon, 1987; Cheddadi et al., 1998). As pointed by Reichert

and Borg (2008), all these parameters have a major influence on the development of supergene non-sulfide zinc deposits. Thus, the Moroccan High Atlas represents a natural laboratory to understand the link between uplift, structure, climate conditions and oxidation processes of sulfide deposits.

This study focuses on six ore deposits or prospects throughout the Moroccan High Atlas. We present field observations of macrostructures and try to decipher the relationships between the protore, the non-sulfide zone, and the host rock. We also give details on the mineralogical assemblages using multi-disciplinary tools for identification and quantification of mineral compositions. All these original results enable us to propose a model that explains, at all scales, the transformation from a sulfide ore, to a non-sulfide ore. We also advance guidelines for future exploration in the Moroccan High Atlas or mine extension.

## 2) Geological setting and brief outline of the Zn-Pb mineralization events

### 2.1) The Moroccan High Atlas

The Atlas Mountains extend from Morocco to Tunisia, with significant lateral variations of altitudes. The Moroccan segment of the Atlas includes the Middle Atlas to the north, and the High Atlas, in central Morocco. The High Atlas is bounded by the Variscan Meseta and the High Plateau to the north, and the Precambrian Anti-Atlas massif with its Paleozoic cover to the south (Fig. 1).

The High Atlas consists of Mesozoic to Cenozoic sedimentary rocks covering a Precambrian to Paleozoic basement, which experienced deformation related to the Variscan orogeny (Piqué and Michard, 1989). Inheritance of Paleozoic structures is extremely important for the geometry of the rifting episode related to the opening of the Tethys and the Atlantic Ocean (Laville and Piqué, 1991). The opening of the Mesozoic basins is controlled

by ENE-WSW trending normal faults, whose chronology remains disputed (Laville et al., 2004; Frizon de Lamotte et al., 2008). Detrital rocks of various grain size and evaporite mainly compose the Triassic rocks (du Dresnay, 1988; Piqué, 1994), which also comprise basalt and dolerite lava flows related to the Central Atlantic Magmatic Province (Verati et al., 2007). Carbonates of the Lower Liassic platform post-date the Triassic rift and grade upward into marl, limestone and calcareous turbidite. This abrupt transition attests to a tremendous increase of subsidence, which can be explained by a second rifting episode between mid-Liassic and Middle Jurassic or Dogger (Warme, 1988). The sedimentary filling of the basin is followed by a regional uplift (Saddiqi et al., 2009) and a marine regression at the end of the Middle Jurassic, with deposition of continental red beds (Charrière et al., 2005) and contemporaneous magmatism (Brechbühler et al., 1988; Laville and Piqué, 1992). Afterwards, the region was completely emerged until the Cretaceous, when sedimentation resumed with deposition of red sandstone and limestone. The establishment of a Late Cretaceous carbonate platform marks a short but major Late Cenomanian-Turonian transgression event (Haddoumi et al., 2008), since continental sedimentation is recorded again at the end of Cretaceous, during the Paleocene (Charrière et al., 2009) and until the mid-Eocene (Herbig and Trappe, 1994).

Presently, the Moroccan High Atlas displays folds and NE-SW to ENE-WSW striking thrusts (Fig. 2A). Wide and open Middle Jurassic-cored synclines are separated by narrow Lower Jurassic-cored anticlines (Fig. 2B). Thrusting may also affects the anticline hinges, exposing the underlying Triassic strata, which have experienced intensive deformation. At depth, the thickness of the crust is remarkably stable, except the sharp transition (ca. 7km) between the High Atlas and the northern domains (Arbeloya et al., 2004). The mechanisms of formation of the belt are still debated. Thin-skinned tectonics (Teixell et al., 2003), with the development of a décollement zone within the soft Triassic layers is generally opposed to

thick-skinned tectonics (Frizon de Lamotte et al., 2000), which emphasizes the role of Hercynian structures and suggests that deep crust has also experienced deformation. However, the thick-skinned model seems to prevail in the Moroccan High Atlas (Teixell et al., 2003), whereas the eastern segments of the Atlas display characteristics of thin-skinned tectonics (i.e. Algeria and Tunisia; e.g. Frizon de Lamotte et al., 2000).

In Morocco, the High Atlas corresponds to an intra-continental belt (Mattauer et al., 1977), whose formation has been facilitated by the crustal weaknesses created by the Mesozoic rifting. Inversion tectonics of the Triassic to Jurassic normal faults occurred between Eocene and Quaternary, with alternation of quiet and active periods of uplift (Frizon de Lamotte et al., 2009). The first major compressive event was recorded at the Lutetian-Bartonian transition (ca. 40 Ma), while the present topography is mainly due to a secondary Pleistocene episode. The formation of the Atlas range may originate from the convergence of Africa and Europe, although the role of slab-roll back in the Mediterranean regions should not be ignored (Jolivet and Faccenna, 2000). Shortening is evaluated to twenty-six kilometers only (ca. 10 %). Such weak values are hardly compatible with the present topography of the belt (Frizon de Lamotte et al., 2009). Therefore, a complementary role of the asthenosphere must be considered (Missenard and Cadoux, 2011).

## 2.2) The Zn-Pb ore deposits of the Moroccan High Atlas

### 2.2.1) The Zn-Pb sulfide deposits

The Zn-Pb ore deposits of the Moroccan High Atlas belong to the Zn-Pb province of the circum-Mediterranean Sea and Alpine Europe (Rouvier et al., 1985). The numerous prospects and ore deposits of High Atlas (Ovtracht, 1978) make this region of economic

importance for the extraction of base metals (Fig. 2A). Mouguina (2004) recognizes two metallogenic periods for Zn-Pb sulfide ore deposition:

- the Lower Jurassic (the Lias). Ore bodies are marked by stratiform lenses of Zn-Pb-Fe sulfides and have been considered as syngenetic (Agard and du Dresnay, 1965; Emberger, 1965; Bazin, 1968; Auajjar and Boulegue, 1999). The paleogeography with horst and graben, and the Liassic normal faults have largely controlled the ore formation. Hence, Leblanc (1968) considered that lithological and petro-physical characteristics of the Lower Jurassic massive limestone might have played a role for the localization of the ore bodies. Mouguina (2004) has also suggested a genetic link with the contemporaneous magmatism, which has produced gabbro, basalt, and dolerite.

- the Middle Jurassic (the Dogger). Ore-bearing structures are closely related to the emplacement of basic magmas, and the tectonic inheritance of the region. Ore is chiefly disseminated in gabbro, with an early Cu-Ni mineralization (Chèvremont, 1975) and a later Zn-Pb episode (Caïa, 1968) of hydrothermal origin. In the calcareous host rocks, ore bodies contemporaneous to the Middle Jurassic magmatic intrusions are reported (Mouguina, 1992; Mouguina et al., 1999).

The presently available data cannot ascertain the origin of the Early Jurassic ore deposits, and therefore their attribution to MVT or Sedex types is still debated. Conversely, based on structural and mineralogical investigation, Mouguina and Daoudi (2008) have proposed that some of the Middle Jurassic Zn-Pb ore deposits of the High Atlas could be similar to MVT, like those of Touissit and Mibladen described to the north of the eastern High Altas (Dagallier, 1977; Wadjinny, 1989).

### 2.2.2) The Zn-Pb non-sulfide deposits

Based on several studies in the sixties, Ovtracht (1978) published a model trying to explain the genesis of supergene Zn-Pb ore deposits in the Moroccan High Atlas in a single step. He has considered a complex karst system with ascendant and descendant fluids. He also advanced that coexistence of sulfide and non-sulfide minerals were not caused by mineral replacement, and were rather due to the tremendous variations of redox characteristics directly controlled by the surficial and deep waters. The meteoric water contributes to the formation of the supergene karst, which mainly hosts oxides, silicates, carbonates (and their hydrated equivalents) and per descensum barren clays as well. Conversely, hydrothermal fluids have formed the hypogene karst made of massive calcite, the miscellaneous sulfides, and the newly formed metal-enriched clays (Ovtracht, 1978). In this holistic view, all the minerals were considered as the result of a single cycle of fluid flow. Hence, the geochemical boundary between the two fluids represents a propitious environment for metal deposition.

The model of Ovtracht (1978) was not in accordance with previous observations, made throughout the High Atlas, which alternatively advanced a two-step evolution. In the Bou Dahar massif, Agard and du Dresnay (1965) stated a link between the non-sulfide stratiform and vein deposits and the Atlas compression during Tertiary, and therefore an obvious diachronism between sulfide deposition and sulfide oxidation. At Bou Arhous, Leblanc (1968) advanced that tectonic features, such as thrusts, might have facilitated the infiltration of meteoric water and the oxidation of the primary ore. At Tizi N'Firest to the south of the city of Rich (Fig. 2A), Bazin (1968) hypothesized a genetic connection between non-sulfide mineralization and karst network geometry. He also suggested that the local variations of the water table have controlled the geometry and the mineral content of the supergene ore deposits. More recently, Mouguina et al. (1999) have studied the Tazoult deposit in Central High Atlas and hypothesized that in-situ oxidation of the primary sulfide

deposit coexists with zinc remobilization largely controlled by the hydrodynamics of the karst network.

## 3) Local geological context and main features of the studied deposits

The following presents our macroscopic observations from six sites of supergene non-sulfide ore deposits distributed in the Moroccan High Atlas. For Beni Tajite, Bou Arhous, and Tizi n'Firest deposits, we complement our observations with the respective works of Agard and du Dresnay (1965), Leblanc (1968), and Bazin (1968). In this study, the term "calamine" is used to describe any non-sulfide zinc ore, without genetic or mineralogical implications.

### 3.1) The Toulal prospect

The Toulal prospect (32.30°N, 3.99°W) is currently at exploration stage by Managem. This site is located near the city of Toulal, 30 km to the east of the city of Rich (Fig. 2A). It corresponds to the northeastern periclinal termination of an ENE-WSW trending narrow anticline (Fig. 3A). The northern and southern limbs display Pliensbachian thin-bedded limestone, whereas the Upper Sinemurian para-reefal massive black limestone forms the fold hinge. In detail, the bedding variations of strata suggest subsidiary folds within the anticline, which present slightly overturned strata to the north (Fig. 3B). Triassic shale that constitutes the core of the anticline does not crop out.

The present structure also displays minor effects of collapse tectonics. A detachment fault separates the autochthonous rocks of the fold hinge from the allochthonous Upper Sinemurian layers (Fig. 3C). Detachments are also revealed by a deformed drusy calcite. Syn-compressive faults are rarely visible except at the periclinal termination, where thrusting is

documented by top-to-the-west shear criteria in the cataclasite and breccia (Fig. 3D). This tectonic breccia contains fragments of limestone and white massive calcite. To the west, the thrust progressively evolves to a tight anticline marked by a cataclastic zone as well (Fig. 3A). White massive calcite (early calcite) occurs as extrados-type fractures (fractures distributed radially in the outer part of a fold) fillings of the fold (Fig. 3E), locally capped by rocks of the allochthonous unit. This subsidiary anticline displays parasitic and disharmonic folds, which have been repeatedly observed in the overlying Pliensbachian strata. The limestone displays stylolites occurring parallel to the bedding.

Calamine veins (in this study, we use "veins" only to describe the geometry of the deposits without any genetic inferences related to extension setting) are located in the cataclastic zone that affects the Upper Sinemurian black limestone (Fig. 3A). Calamines clasts are enclosed in a tectonic breccia, which contains decimeter-sized fragments of black limestone cemented by banded calcite. This cement is contemporaneous to the late drusy calcite, which coats the calamine orebody. The veins form N70°E striking steepened boudin-like lenses (Fig. 3F), which crosscut the extrados fractures filled by early white calcite. The trend of the veins and the bedding of the limestone strata are concordant. Various facies of calamine have been observed, such as vacuolar, banded, or massive. The calamine is mainly red or ocher due to oxidation, but grey calamine has also been observed in the dumps. In vacuolar facies, we have observed geodes with a fibrous coating, and red to black spots corresponding to in situ oxidized sulfides. Preserved sulfides (galena and sphalerite) enclosed in the red calamine have been found in the dumps. Banded calamine commonly covers the inner walls of the cavities, locally filled by Zn-poor internal sediments grading 4-5 ZnO wt%. Internal sediments (Fig. 3G), filling metric to decametric cavities comprise marl and calcareous shale with horizontal bedding and grain size variations.

3.2) The Bou Arhous ore deposit

The Bou Arhous ore deposit (32.27°N, 3.76°W) is a part of the Jbel Bou Arhous, which also hosts the Iboughalene and Atchana Pb-Zn-Mn mines and numerous miscellaneous prospects (Fig. 4A). This range presents an ENE-WSW trend and extends over thirty kilometers. It corresponds to an anticline and exhumes Triassic and Liassic strata. Folding is accompanied by faulting along the "Grand Accident" top-to-the-south thrust, which parallels the trend of the range and represents a boundary between the different Liassic sedimentary facies (Leblanc, 1968). To the west, the fold is slightly recumbent and the northern limb is overturned (section A-A' of Fig. 4B). The Triassic rocks crop out along the steepened "Grand Accident" fault and consist of variegated shale and marl (with beds of gypsum), which have been crushed and sheared along the thrust (Fig. 4C). The fold hinge has been eroded, and some allochthonous horizontal strata bounded by a gravity-driven detachment fault locally hide the autochthonous series and the "Grand Accident" thrust (section B-B' of Fig. 4B). In the central part of the Jbel Bou Arhous (section C-C' of Fig. 4B), both limbs are overturned and the anticline hinge is also lacking. To the east, back-thrusts are largely developed and a fold hinge with horizontal strata is visible (section D-D' of Fig. 4B). To the south, the Sinemurian strata form a shallow dipping monocline, covered by two Upper Sinemurian coral paleo-reefs, and Pliensbachian marl and limestone (Fig. 4A).

The Bou Arhous zone was prospected in the early sixties by the BRPM (Bureau de Recherches et de Participations Minières). Managem has been exploited the mine since the early 2000's. Reserves have been estimated at 250 kt grading 4% Pb and 16% Zn. The whole mineralization is located in the footwall of the "Grand Accident" fault (section C-C' of Fig. 4B). Steepened plans coated by hydrozincite support a steep N-S trending striation (Fig. 4D). The thrust and its satellite faults as well, often bound crushed red clays and gypsum (Fig. 4E),

similar to those present in the Triassic series. Sinemurian limestone is also faulted, as revealed by the occurrence of breccia close to the orebodies. At the surface, ore-bearing E-W trending veins parallel the anticlinal axis and the "Grand Accident" fault (Fig. 4F). At depth, the veins connect with various-sized conduits and holes (up to 40 metres) to form a 120m-thick complex karst network that, at minimum, extends over 18,000$m^2$. Some veins can reach ten meters in thickness and/or in width. Veins steeply dip to the north, and are often concordant to the bedding of the host limestone. The host rocks of the ore bodies strictly correspond to the Sinemurian black limestone that includes reefal and para-reefal facies. No significant ore bearing minerals except the Iboughalene Mine are reported in the northern hanging-wall of the fault; hence, the "Grand Accident" thrust is not only a boundary for sedimentary facies, but it also represents the northern limit of mineralization (Fig. 4A).

The deposit displays a vertical zonation of Zn-bearing minerals distribution. The upper parts of the mine show the occurrence of non-sulfide zinc minerals, such as willemite, hydrozincite, hemimorphite and smithsonite. Willemite, distributed according to diffuse veinlets or massive patches, constitutes a main Zn-bearing phase (Leblanc, 1968). In deeper levels, sulfide minerals (galena, sphalerite) are prevalent and they display intricate relationships between with white calcite in the veins (Fig. 4G). To the west, the collapsed Liassic strata (section B-B' of Fig. 4B), which cap the autochthonous limestone hosting mineralization, have preserved the Zn-Pb sulfides of the protore from oxidation (Leblanc, 1968). Veins are often associated with E-W trending barren veins filled by white calcite patches (Fig. 4G).

Karst cavities may be filled by internal sediments, which are visible in the galleries and at the surface as well (Fig. 4H). These sediments present horizontal bedding and are mainly marl and shale. They also contain some calamine and host limestone fragments of various sizes. The wall of some cavities can be striated, suggesting karst-related collapse of

limestone boulders. Leblanc (1968) noticed cavities filled by clays. Two types of clay may be distinguished and should not be mistaken for the Triassic red shale. The reddish thin-bedded clays (mainly montmorillonite) are totally barren (Leblanc, 1968), although they may contain fragments of calamines (e.g. willemite) and black limestone. Conversely, white and granular clays (mainly illite and sauconite) are associated to the Zn non-sulfides minerals. At depth, these clays may contain up to 23% of Zn and were therefore categorized as sauconites (Gaudefroy, 1959).

### 3.3) The Tadaghast ore deposit

The Tadaghast ore deposit (31.63°N, 6.61°W) is a part of the Jbel Tadaghast, situated in the central part of High Atlas, at ca. 30 km to south of city of Azilal (Fig. 2A). This region displays a complex architecture due to the numerous faults that have exhumed the Paleozoic basement. Near Tadaghast, an E-W trending major top-to-the south thrust separates the Lower Jurassic strata from the thick Ordovician to Triassic series. The Tadaghast ore deposit is situated in the southern limb of an open anticline, and strata regularly dip at 30° to the south. The Liassic formations include Pliensbachian beige marl and limestone, and Sinemurian black para-reefal limestone with intra-formational breccia (Fig. 5A). The Sinemurian limestone has experienced intense karstification with the development of a typical limestone pavement and small sinkholes. Grikes are filled by internal sediments, which present horizontal bedding (Fig. 5B). At the surface, the limestone is crosscut by N-S trending fractures filled by massive white calcite (Fig. 5C) showing euhedral crystals. Kinematic markers are not clearly visible. N-S trending fractures are reactivated to form a breccia containing fragments of the black limestone cemented by drusy or collomorphic calcite (Fig.

5D). This calcite is also observed in subsidiary E-W trending fractures that dextrally offset the N-S trending breccia zone.

The Tadaghast mine is currently operated by Managem and has produced ca. 69 kt of ore grading 18% Zn. The reserves are estimated at ca. 29 kt of ores grading 25.7% Zn. At depth, ore bodies seem to be distributed according to 3 structural directions, N-S trending fractures, E-W trending fractures and horizons paralleling the stratification attitude (Fig. 5G).

- The N-S-trending fractures are usually filled by calamines, but commonly display breccia with fragments of Sinemurian limestone, calamine (smithsonite and hydrozincite), internal sediments and massive white calcite. Some cavities show a sedimentary infill of marls, partly recycling the aforementioned elements of the breccia. This pattern may suggest several episodes of karstification. Finally, other N-S-trending fractures contain clasts of massive white calcite cemented by banded calcite, whose crystals display a centripetal growth. This late calcite coats the wall of the calamine veins, but can also be the last drusy infilling of the veins. Locally, the latest internal sediments postdate this banded calcite.
- The E-W trending fractures, which include banded and/or vacuolar red calamine present the highest Zn content (up to 50%). The veins display a pinch-and-swell morphology and their thickness may vary from several centimeters to five meters. These veins crosscut the N-S trending fractures with white massive calcite infilling (Fig. 5E). The corresponding offset is of dextral kinematics and may reach 40 cm.
- The horizons are concordant to the bedding of Sinemurian black limestone. They display elongated lenses of sulfides (sphalerite, galena and pyrite). The sulfides have been partly replaced by white and red calamine (Fig. 5F). Galena seems to be residual within the massive calamine, whereas oxidation of sphalerite is in progress. These horizons that can reach up to 4 meters thick are always crosscut by the N-S and E-W trending fractures, which never contain galena.

The schematic 3D diagram (Fig. 5G) gives a synoptic outline of the relationships between the aforementioned lithologies and structures. The intersection of these three types of heterochronous fractures forms large cavities, which are targeted by the mining company.

### 3.4) The Beni Tajite ore deposit

The Beni Tajite mine (32.31°N, 3.45°W) is located near the city of Beni Tajite (Fig. 2A) in the southwestern part of the Jbel Bou Dahar, which also hosts numerous Zn-Pb ore deposits (Agard and du Dresnay, 1965). This WSW-ENE range chiefly corresponds to a preserved Pliensbachian coral reef and covers a large surface (45km x 20km) (Agard and du Dresnay, 1965). Whereas a Paleozoic paleo-relief crops out in the folded central part of the Jbel Bou Dahar, the southwestern domain rather displays a tabular architecture, marked by a rim of coral-rich limestone surrounding fine-bedded limestone originally formed in a lagoon (Agard and du Dresnay, 1965).

The mine, which extends to a depth of 170m was operated by Peñarroya (SMMP) in the first half of twentieth century until its closure in 1962. Local operators currently exploit the mine and production is estimated at ca. 300 kt of ore grading 22-30% Zn. The ore mainly occurs in E-W trending veins or in NW-SE trending sub-vertical fractures. Fracture intersection represents zones of economic interest. Sulfides (galena, sphalerite and pyrite) are frequent at depth. Translucent honey-colored sphalerite is disseminated within fossiliferous limestone and seems to fill geodes (1 to 5 cm in diameter). Galena is repeatedly associated to rhombohedral white calcite; this may represent an original karst filling that hosts the sulfides prior their oxidation (Fig. 6A). Such karstic structures seem to predate the formation of sulfide minerals as inferred by the banded calcite, whose crystals show centripetal growth, that separates the sulfides from the Lower Liassic limestone (Fig. 6A). In the shallow levels,

the banded red calamine (mainly smithsonite) is distributed according to a complex network of veins (Fig. 6B). In vacuolar parts, botryoidal masses of hemimorphite coat the bands of smithsonite. Locally, decimeter-thick bands of white hydrozincite coat the wall of the red calamine veins (Fig. 6B). Hydrozincite is also visible as a cement of the limestone breccia.

### 3.5) Other ore deposits

The Aït Labbes ore deposit (32.38°N, 4.38°W) is situated 15 km to the northeast of the city of Rich (Fig. 2A). Local geology is characterized by an ENE-WSW trending fault cutting a narrow anticline that has exhumed Triassic variegated marl and massive Sinemurian para-reefal limestone. To the northeast and to the southwest, this anticline evolves toward a complex folded structure with narrow anticlines bounding large synclinal plains that expose mid-Liassic to Dogger formations. At Aït Labbes, the bedding of limestone is steepened and the fold hinge has been eroded. The mine is operated by local miners and has produced 200 kt of ores, although the Zn content ranging from 3 to 30% shows huge spatial variations. The ore body, which is known to extend over ca. 100 meters of depth, occurs within ENE-WSW vertical veins that parallel the bedding of limestone and the ENE-WSW trend of the fault. Boudin-like calamine ore bodies are also distributed along this fault, which is offset by subsidiary N-S trending dextral strike-slip faults. Isolated masses of sulfides (galena and sphalerite) are preserved within the red calamine composed of smithsonite and clays. Gypsum coating on limestone and impregnation within limestone have been locally observed. Various types of calcite fill the fractures in the host limestone. Large euhedral crystals of beige calcite occur in the irregular cavities of the limestone. This type of calcite predates the calamine orebodies (Fig. 6C), as well as a secondary generation of white calcite, whose crystals present a centripetal growth. This late type of translucent banded calcite, postdating the calamine

vein, cements limestone and calamine clasts in a cockade breccia (Fig. 6D). Internal sediments of barren marl present horizontal bedding, and they locally recycle some fragments of calamine.

The Tizi n'Firest ore deposit (32.18°N, 4.29°W) is a part of the Jbel Tizi n'Firest, located 20 km to the southeast of the city of Rich (Fig. 2A). Local geology of this range consists of an anticlinal ridge, whose axis parallels an E-W trending thrust, namely the "Accident Méridional" (Bazin, 1968). This thrust has probably recorded huge horizontal displacements toward the south, since the Triassic rocks are juxtaposed with the Bajocian strata. Hence, the southern limb of the Tizi n'Firest box fold is lacking. To the east, this structure divides into two faulted anticlines bounding a large synclinal plain that exposes Middle Jurassic formations. At Tizi n'Firest, folding has exhumed Triassic marl and basalt, as well as Sinemurian massive limestone hosting the ore. The mine has always been operated by locals and comprises three galleries over a depth of ca. 50 meters. The ore body represents a vast cavity that dips to the north at 70°. Its maximal thickness is 15 meters giving it an oblate shape. The cavity and its numerous digitations are partly filled by clays, which show horizontal stratification. Calamine veins striking parallel to the E-W major thrust have also been recognized in the galleries. Banded calcite may coat the wall of the cave and locally presents botryoidal shapes. The clay is often barren, but Zn-rich illite is also present (Bazin, 1968). This clayey infill contains isolated patches of cerussite-rimmed galena often associated with euhedral crystals of white calcite. Banded smithsonite forms concretions recycled in the clay.

## 4) Analytical procedures

During the two field trips, 59 samples have been collected in the galleries and in the dumps close to the mines. One to three thin sections were prepared for 35 out of 59 samples. Polished thin sections have been first observed using a Leica DRMX petrographic microscope (transmitted and reflected light modes). Miscellaneous techniques for qualitative and quantitative determination of the mineral content were carried out to complement our identification of the paragenesis for each ore deposit.

X-ray diffraction has been carried out on eight samples to get a preliminary identification of the mineral content. For each sample, rock powder was first crushed in an agate mortar and then placed into a glass capillary tube with a diameter of 0.3mm. Instrumentation hosted at Institut des Sciences de la Terre d'Orléans (ISTO) consists of an INEL XRM3000 diffractometer in transmission mode coupled to an INEL CPS 120 curved position sensitive detector. We used CoKα radiation at 1.78897Å with a step scan of 0.03° (2θ) in the 3-120° (2θ) interval. Acquisition time ranges from 120s to 180s, depending on samples. INEL Windif software package was used for data processing.

Raman spectroscopy enables us to identify specific mineral phases and reveal their relationships. Selected polished thin-sections were fixed to a piezo-electric table itself coupled to a motorized table. We used the WITecAlpha500 RA confocal micro-Raman spectrometer coupled with an Atomic Force Microscope (AFM), working with a green laser (Nd:YAG frequency doubled, λ = 532nm) and a near IR diode laser (λ = 785nm). This instrumentation hosted at Centre de Biophysique Moléculaire of CNRS Orléans allows for making individual analyses, and composition mapping with a resolution of less than 1µm. For identification, we have used CrystalSleuth software package and several databases including RRuff.

Complementary observations and analyses were carried out using JSM-6400 JEOL Scanning Electron Microscope (SEM) hosted at ISTO. Polished thin-sections have been first coated by a thin carbon layer. Acceleration voltage and beam current were 20kV and 8nA,

respectively. IdFix Software package was used for data processing. Back-scattered electrons (BSE) imaging mode was used for evaluating composition variations at microscopic scale, whereas the texture of clayey material was examined with secondary electrons (SE) imaging mode. The SEM system is coupled to an Energy-Dispersive X-ray spectrometer (EDS) to make qualitative determinations of the mineral composition.

To get quantitative composition of selected minerals, we have used a Cameca SX50 electron microprobe hosted at BRGM/ISTO equipped with four wavelength dispersion spectrometers (WDS). On carbon-coated polished thin-section, we operated at 15kV with a beam current at 10nA for carbonates and 20nA for sulfides. The spot resolution is ca. 1µm. Silicates, oxides, and pure elements were used as standards. For sulfides, we only retained individual analyses with a total ranging between 97 and 103%, whereas for carbonates, the micro-scale association with oxides prevents from establishing range of confidence on total. We have also evaluated the statistical significance of our dataset at 95 and 99% of confidence level, by checking that the time-integrated difference between each sample peak and the background is higher than two or three times the standard deviation of the time-integrated count of the background, respectively. Details are given in Table 1 caption. In addition, X-ray intensity hyperspectral mapping were realized to disclose the specific textures caused by the chemical features of minerals.

## 5) Mineralogical and textural evolution of calamine-type deposits of the Moroccan High Atlas

### 5.1) The Toulal prospect

Sinemurian host limestone is characterized by a microcrystalline texture. Locally, large crystals of calcite due to recrystallization occur and coexist with veinlet of calcite. The

rock experienced intense fracturing, which has been largely described at macroscopic scale. Beside the two generations of calcite (white massive and banded drusy), a complex network of small fractures contains pinkish carbonates, which have been identified as dolomite by X-ray diffraction (Fig. 7A). Such infill of dolomite remains very minor.

Galena is the main remnant minerals of the protore (Fig. 7B). Galena is deformed as inferred by the geometry of the triangular pits formed during polishing and is bounded by a botryoidal-rhythmical rim of cerussite growing toward the sulfide grain. Finely powdered galena and covellite are commonly found in the cerussite crusts (Ramdohr, 1969). Galena (Gal I in Table 1) presents a Bi content up to 7600 ppm, but no significant Ag content. Except the small inclusions in galena, pyrite is transformed into goethite and hematite, which represent the rim and the core of the pseudomorph, respectively (Fig 7C). Locally, pseudomorphism is only partial since: 1) pyrite is preserved, and 2) iron oxi-hydroxides can occur at a disordered hydrous state, namely the ferrihydrite. In some extreme cases, the core of the pseudomorph displays small scales forming a rosette. Using Raman spectroscopy, we have also identified lepidocrocite (γ-FeO(OH)). Raman composition mapping (Fig. 7D) shows that lepidocrocite occurs in the core of the pyrite pseudomorphs, bounded by a succession of two irregular rims of hematite and goethite. Raman spectroscopy has revealed that the rim around galena contains cerussite, but also anglesite, which occurs exclusively close to pyrite pseudomorphs (Fig 7D). Like pyrite, sphalerite is rarely preserved except as inclusions within the galena (Fig. 7B). In addition, isolated relics of sphalerite, associated with galena and pseudomorphed pyrite, have been identified in the smithsonite of the calamine ore (Fig. 7E). This sphalerite presents slightly variable (ca. 20% for RSD value; see Table 1) Fe and Cd average content of 1.20 wt% and 0.21 wt%, respectively (Table 1). Sphalerite relics are partly cemented by a secondary type of galena (Gal II, Table 1) and

covellite, also occurring as disseminated within the smithsonite. The type II galena presents a moderately lower content in Bi (6000 ppm) than the type I galena (Table 1)

In the non-sulfide ore, smithsonite is the dominant phase and has been identified by X-Ray diffraction (Fig. 7F), Raman spectroscopy, and EDS. Smithsonite is usually associated with pseudomorphed pyrite and forms massive aggregates of rhombohedral crystals, which experienced oxidation revealing growth banding (Fig. 7G). These aggregates (Sm I) are encrusted by rhythmical bands of rhombohedral smithsonite (Sm II), which are locally colored by iron oxi-hydroxides (Fig. 7H). The differences between the two generations of smithsonite are also visible on WDS composition maps, since aggregates of type I smithsonite are depleted in zinc (Fig. 7I) and enriched in iron (Fig. 7J), with respect to the encrustation of type II smithsonite. Indeed, the average Fe content in type I smithsonite is 9.28 wt% FeO but highly variable, whereas this value is 0.32 wt% FeO in type II smithsonite (Table 1). It is worth noting that smithsonite from Toulal ores contains Mg content more than 0.5 wt% MgO (Table 1), which could be related to the local occurrence of dolomite.

Following smithsonite accumulation, several minerals such as, descloizite, psilomelane, sauconite and hydrozincite have been formed contemporaneously (Fig. 8A). Descloizite (lead zinc vanadate hydroxide) that was identified by Raman spectroscopy and EDS (Fig. 8B) forms concretion and rarely flakes associated with iron oxi-hydroxides encrustations. Psilomelane is common and encrusts the mass of smithsonite. At microscale, these aggregates present a botryoidal layered structure (Fig. 8C) and seem to contain a microcrystalline association of coronadite (lead manganese oxide) and chalcophanite (zinc iron manganese hydroxide), as inferred by EDS (Fig. 8D). X-Ray diffraction and EDS have also revealed the occurrence of Zn clays, namely sauconite in some geodes rimmed by drusy smithsonite (Figs. 8E and 8F). A fissure network, similar to mud cracks characterizes the internal texture of this clayey infill. Hydrozincite (zinc carbonate hydroxide) was rarely

observed in macroscopic samples but is frequent under microscope; Raman spectrometry confirms its occurrence. Hydrozincite forms localized white impregnations of stippled patches that replace smithsonite (Figs. 8G and 8H). The remaining oxidized parts higlight such pseudomorphs after smithsonite.

After the formation of the different phases mentioned above, diverse materials have filled the remaining cavities. A second generation of cerussite, occurring as large crystals is locally observed close to the original lead-bearing phases (Fig. 8H). Botryoidal concretions or prismatic crystals of hemimorphite (hydrated zinc silicate hydroxide) are also common (Fig. 8I) and were identified by Raman spectroscopy and EDS. It is worth noting that thin tabular crystals of hemimorphite are not radially arranged in the cavities within the massive smithsonite and the unipolar disposition is consistent with the usual distribution of speleothemes in caves. Geodes were finally filled by calcite, as observed macroscopically. The calcite crystals are large (Fig. 8I) and were distinguished from other carbonates by their Raman spectra. They locally present relics of growth bands that underline rhombohedral crystals with curved faces (Fig. 8I); this may correspond to calcite pseudomorph after smithsonite.

### 5.2) The Bou Arhous ore deposit

As observed for the Toulal prospect, the Upper Sinemurian host limestone has a microcrystalline texture. Nail-head spars of calcite, showing growth bands, fill the rare geodes. Leblanc (1968) has first described the occurrence of quartz needles disseminated in the limestone. The length of needles may vary between 0.1 cm and 1.5 cm. We have locally observed microbreccia displaying cementing of iron oxi-hydroxides, which should not be mistaken for the oxidized pyrite present in the limestone.

The protore mainly includes galena, which has been deformed as revealed by the geometry of the triangular pits (Fig. 9A). As shown macroscopically, the galena is frequently associated with massive calcite exhibiting well-crystallized sections. In thin sections, the curved aspect of the cleavage traces reveals that calcite also experienced deformation (Fig. 9B). Galena is always coated by botryoidal masses of cerussite that form rhythmic bands (Fig. 9C). Cerussite, identified by Raman spectroscopy and EDS incorporates a finely powdered galena. Cerussite also pervades into cracks formed after cleavage traces of the calcite crystals.

Willemite (zinc silicate) predominates in the calamine ores, which also contain the aforementioned galena and cerussite, sphalerite, quartz, and smithsonite (Figs. 9D and 9E). In addition to the typical various bright colors ($2^{nd}$ order of Michel-Levy Birefringence scale) (Fig. 9F), Raman spectroscopy and EDS (Fig. 9G) have confirmed the presence of willemite. Willemite rarely occurs as sprays of tabular crystals; it commonly forms a massive material that cements the relics of the protore (Figs. 9F and 9G). The small sphalerite relics are pseudomorphed by willemite, and locally present structures due to cementation, such as a very thin coat of sulfides (galena, covellite). Quartz needles of ca. 0.5 mm in length are common in the calamine ore (Fig. 9H). However, contrary to those observed in the host limestone, the quartz needles of the calamine ore have been broken into small fragments or display microboudinage. They are incorporated in a cement of willemite associated to smithsonite. In other samples, the calamine ore is mainly composed by euhedral rhombs of smithsonite. Pseudomorphed pyrites are abundant in the smithsonite-rich concretions, and usually display hematite and goethite in the inner and outer parts, respectively.

Locally, goethite coats the massive aggregates of smithsonite and oxidized pyrite. Goethite also occurs within cavities to form rhythmically banded accumulations of concentric shells. Some cavities are filled by clayey material with a high Zn content (Fig. 9I). SEM imaging reveals the complex arrangements of the flat sheets. As observed on hand samples,

hydrozincite is very common and forms concretions with a fibrous radial structure that developed on smithsonite aggregates (Fig. 9J). The rhythmical succession of these concretions locally gives a laminated aspect to the calamine. It is worth noting that quartz needles are preserved during the whole supergene process, since relics may be found in the smithsonite aggregates impregnated by hydrozincite. The final infilling of cavities is composed by hemimorphite prismatic crystals, which usually coats hydrozincite concretions (Fig. 9J), followed by an accumulation of small calcite rhombs identified by Raman spectrometry.

### 5.3) The Tadaghast ore deposit

The Sinemurian host limestone is composed by sub-rounded clasts cemented by small crystals of calcite. The clasts are mainly biogenic remnants such as corals fragments, but intraclasts of carbonate with microcrystalline texture are also common.

The sulfides are sphalerite, galena, and pyrite. As described in section 3.3, sphalerite is well preserved in the horizons that parallel the host limestone bedding. In the massive sulfide, sphalerite is locally translucent due the low Fe and Cd contents that average 0.86 wt% and 0.42 wt%, respectively (Table 1). However, the alternating opaque and translucent bands (Figs. 10A and 10D) suggest growth and trace elements content zoning (Figs. 10B and 10C). Indeed, the Fe (Cd) content varies from 0.4 (0) wt% to 2.1 (1.6) wt% along the transected crystals of sphalerite, and Fe and Cd present an obvious positive correlation (Figs. 10G and 10H). In addition, Fe and Cd seem to have been incorporated in the sphalerite structure according to particular crystal faces (Figs. 10B and 10C). Conversely, sphalerite crystals exposed to oxidation present an orange rim, which also penetrates along fractures (Figs. 10E). This band is clearly depleted in iron (Figs. 10F and 10I) and in Cd, moderately (Fig. 10I). The

composition of the sphalerite relics isolated in the calamine ore is not very different for the Zn, Fe, and Cd content, but little enrichment in Cu (0.32 wt%) is recorded (Table 1). Like sphalerite, galena is not deformed and present small inclusions of sphalerite. Identically, sub-rounded galena inclusions may be found in sphalerite (Fig. 10E). Galena inclusions present a positive anomaly in Bi that averages 7600 ppm (Table 1). Pyrite occurs as large patches that seem to cement the other two sulfides. Spherulitic pyrite is also observed in inclusion within sphalerite. A mineral mixture is locally observed in the fractures or in the voids between the preserved sulfides of the protore (Fig. 10J). Infilling material consists of bipyramidal prismatic crystals of quartz incorporated in a clayey-carbonaceous matrix. After bedding correction of the sample, only the cavities looking upward are filled by clayey material. Such polarity supports gravity infilling of the porosity and internal sedimentation processes. Pyrite spherulites seal the contact between the host sulfide and the Zn clays; therefore, they postdate this episode of internal sedimentation.

Smithsonite is the major component of the calamine ore. It generally forms massive concretions of translucent rhomboidal crystals with curved faces (Fig. 10H), which reapeatedly infill the boxworks left by dissolved sphalerite (Fig. 10K). Smithsonite from Tadaghast ore is almost pure, with low Mg content (Table 1). Although the Fe average content is lower than 0.5 wt%, WDS composition map obtained by EPMA reveals local variations and zoning according to growth bands (Fig. 10I). In the preserved parts of the protore, smithsonite penetrates into the fractures and at grain boundaries. The fragmentary geometry of the sulfides, especially the pyrite, evokes hydraulic brecciation. Locally, the smithsonite cement also incorporates broken quartz, which originates from prismatic crystals (Fig. 10L). In the evolved calamine ore, smithsonite can include sphalerite that has been preserved from oxidation. These relics always present a thin coat of galena (partly transformed into cerussite) and covellite (Fig. 10M). EDS has also revealed that covellite may

be locally enriched in Cd (Fig. 10N), probably due to microscopic greenockite (cadmium sulfide).

Oxidation has also affected smithsonite, since iron oxi-hydroxides have rhythmically pigmented the rhombs, according to growth banding (Fig. 10F). Oxidized parts are highly depleted in Zn up to ca. 22 wt% (compared to the 52% Zn content of for an ideal smithsonite) and enriched in Fe up to ca. 22 wt% (Table 1). Goethite also fills geodes within smithsonite and occurs as rhythmical concretions, with concentric textures. In the upper levels of the mine, smithsonite is replaced by hydrozincite, which forms rhythmical masses. Hydrozincite is usually white, but can also be colored by iron oxi-hydroxides

Drusy smithsonite may locally cover the hydrozincite concretions. Hemimorphite is also common, either infilling geodes or directly replacing sphalerite. Cavities may be filled by large crystals of cerussite, which were identified by Raman spectroscopy. This type of cerussite should not be mistaken for the patches of early cerussite dusted by microscopic galena. Late cerussite is generally associated with calcite and smithsonite. Carbonates have been distinguished by their Raman spectra.

5.4) The Beni Tajite Ore Deposit

The Pliensbachian host limestone presents broken fragments of corals cemented by calcite (Fig. 11A). The small crystals of calcite that occur within bioclasts reveal local recrystallization. The limestone also contains elongated prisms of euhedral quartz, already described by Agard and du Dresnay (1965).

The protore that is preserved in the deeper levels of the mine is characterized by the association of massive calcite and galena, with rare sphalerite. At the microscale, such aggregates are frequent. Galena is usually deformed and locally occurs as inclusions within

the large crystals of calcite (Fig. 11B). Galena is commonly replaced by cerussite, which forms botryoidal encrustations mixed with dusty galena (Fig. 11C). In the breccia zone, cerussite cements the clasts made by massive calcite. Cerussite was identified using EDS and its composition is almost pure except minor Sr, Ba and Cu contents (Table 1). This latter anomaly may be due to the ultrafine inclusions of covellite, which are frequent in cerussite encrustations (Ramdohr, 1969). Raman composition mapping has revealed that two types of cerussite exist in such armoring textures (Fig. 11D). Type 1 cerussite, which is marked by a relative low intensity characteristic Raman peak at ca. 1055 $cm^{-1}$, occurs in the rhythmical alternations that form the crust. Conversely, type 2 cerussite displays Raman spectra with a relative high intensity Raman peak at ca. 1055 $cm^{-1}$and it is only observed in the non-structured domains of the crust; this may correspond to recrystallization domains. Sphalerite is locally associated to galena, but can also occur within cavities of the limestone. Rare pyrite is either included in sphalerite, or hosted in the limestone.

Though the calamine ore is mainly composed of smithsonite (Figs. 11E and 11F), it commonly contains relics of sphalerite (Fig. 11G). Euhedral crystals of quartz have also been preserved in the calamine (Fig. 11G). Iron oxi-hydroxide pseudomorphs after pyrite are associated with smithsonite, which locally presents evidence for oxidation. Goethite and hematite usually form the outer and inner parts of the pseudomorphs, respectively, but iron oxi-hydroxide have been locally leeched and replaced by smithsonite.

A thin crust of Mn oxides containing Pb and Zn (possibly coronadite and chalcophanite) locally coats the oxidized parts of calamine (Fig. 11H). They form kidney-shaped protuberances, with a rhythmically banded texture. Hydrozincite partly replaces the oxidized calamine. It is characterized by a banded structure, and only euhedral quartz remains identifiable in these hydrozincite masses. Commonly, secondary smithsonite forms botryoidal concretions or rhythmical bands of large crystals (Fig. 11H); it may contain CaO up to 1 wt%

without significant MgO (Table 1). EDS composition mapping has also revealed internal zoning of the Ca content according to growth bands. Within cavities of the calamine ore, clayey material occurs. A late stage of banded calcite, with crystals showing centripetal growth was formed (Fig. 11I).

5.5) Other ore deposits

At Aït Labbes, the protore is mainly composed by sphalerite, which contains sub-rounded inclusions of galena. Pyrite is very common and occurs as nodular aggregates (Fig. 12A). The origin of this fragmentary aspect remains unknown. Locally, these aggregates are aligned and it suggests either infilling of fractures, or cementing of sphalerite. Whatever the formation process of pyrite, its presence seems to localize the replacement of sphalerite by smithsonite, since smithsonite has only been observed at the boundary between sphalerite and pyrite (Fig. 12A). In other samples, sphalerite has been totally dissolved and the calamine ore consists in the association of pyrite and smithsonite. However, this pyrite is rarely preserved and transformed into a mixture of iron oxi-hydroxides (Fig. 12B). Goethite is predominant or rarely forms the rim of pseudomorphs with hematite in the core. Iron oxi-hydroxides also emplaced after smithsonite precipitation, as revealed by the content zoning according to growth banding (Fig. 12C). In extreme cases, all the smithsonite has been replaced by iron oxi-hydroxides, but the original rhythmically banded texture of the carbonate crust remains preserved (Fig. 12D). Later, hemimorphite occurs as large crystals within geodes. It may also replace smithsonite (Fig. 12E). It is worth noting that Fe-enriched growth bands of smithsonite are preserved within hemimorphite crystals. Large crystals of calcite represent the final infill of cavities

At Tizi n'Firest, sulfide minerals of the protore have been rarely observed. Bazin (1968) has described relics of galena rimmed by cerussite, but sphalerite never occurred. Pyrite is very common but rarely preserved. An external rim of goethite surrounding hematite characterizes the pseudomorphs after pyrite. The red calamine ore is composed of an association of oxidized pyrite and smithsonite (Fig. 12F). Euhedral crystals of quartz are locally included in the oxidized aggregates, but small veins of quartz are also described (Bazin, 1968). Smithsonite is pigmented by a mixture of iron oxi-hydroxides or was transformed into rhythmically banded hydrozincite. In other samples, red calamine ore is coated by a secondary generation of translucent smithsonite (Fig. 12F). These drusy crystals predate the deposition of clayey material that fills cavities (Fig. 12F), or the intervening spaces between smithsonite crystals. X-Ray diffraction attests to the presence of sauconite, accompanied by calcite and minor smithsonite and goethite (Fig. 12G). Clays may penetrate the banded hydrozincite and disturb the laminar texture. The clayey material usually shows mud cracks, which have been further filled by calcite and hemimorphite.

## 6) Discussion

### 6.1) Paragenetic sequences of ore deposits: similarities and differences

Based on the aforementioned macroscopic and microscope observations, we have established the paragenetic successions of the identified minerals for each ore deposit (Fig. 13). The following general features are observed:

- The host rocks always correspond to massive limestone with abundant coral fossils. Limestone has formed in a reefal or para-reefal environment commonly close to the transition from the platform to the deep sea (Leblanc, 1968; du Dresnay, 1979). Quartz needles that

originate from a silicification event are described as components of the limestone (Leblanc, 1968) and were found in most of the deposits, whatever the progress of alteration process.

- A protore composed of primary sulfides and massive white calcite is common to the six deposits (Fig. 13). Protore sulfides are galena, sphalerite and pyrite, but their relative proportions may vary. The initial content in sulfides can be different between ore deposits (e.g. pyrite is rare at Beni Tajite but very common in other deposits) or within a same deposit as well. Supergene oxidation emphasizes the variability of sulfides, as, for a given deposit, dissolution of sphalerite and pyrite is more advanced than that of galena in the shallow levels (Jambor, 1994). In addition, the progress of oxidation can be very different between the six sites due to variable water tables, and they now present variably preserved protores. As an example, the primary sulfide horizons are still visible at Tadaghast (Fig. 5F). At Beni Tajite, primary sulfides may occur disseminated in the limestone or within small paleo-caves resulting from host rocks dissolution (Fig. 6A). Conversely, primary sulfides seem to have been completely dissolved at Tizi n'Firest, except remnant galena (Bazin, 1968).

- For each ore deposit, pyrite has been pseudomorphed by iron oxi-hydroxides, with hematite surrounded by goethite. Such replacement textures are typical of supergene oxidation in a neutralizing environment due to carbonate (Chukhrov, 1975). Lepidocrocite was identified only at Toulal (Fig. 7D), and this occurrence is merely due to its atypical mode of formation. Indeed, lepidococrite does not directly result from the transformation of pyrite. It is preferably formed after maturing of a ferric gel (Kosakevitch, 1983). Such gels are repeatedly observed in the pseudomorphs (Fig. 7C) and they may represent a preserved stage of pyrite oxidation.

- As a common feature of all sites, we have observed two successive types of calamine (Fig. 13). On one hand, "red calamine" is composed of the iron oxi-hydroxides-smithsonite association and therefore presents higher Fe content than the latter generation of calamine. The precipitation of smithsonite concretions is often contemporaneous with the formation of

iron oxi-hydroxides. Atypically, black calamine composed of willemite occurs locally at Bou Arhous, but never coexists with the red one. On the other hand, a secondary generation of calamine develops after the red type or is precipitated in karst cavities. This calamine is grey or white due to the lack of iron oxi-hydroxides and contains hemimorphite and translucent smithsonite. The association of hydrozincite with one type or another is not obvious. At Toulal or Bou Arhous, hydrozincite is contemporaneous to the formation of iron oxi-hydroxides, which impregnate the white patches of hydrozincite. Conversely, hydrozincite clearly postdates the red calamine of Beni Tajite ore deposit. Whatever the affiliation of hydrozincite is, a simplistic succession smithsonite I-hydrozincite-hemimorphite±smithsonite II may be advanced for each ore deposit. Like smithsonite, two generations of cerussite have been observed: 1) early alteration of galena (Fig. 11C), and 2) precipitation in druse (Fig. 8H) accompanied by a recrystallization of type I cerussite (Fig. 11D).

- Several minerals, such as descloizite or psilomelane are not very common and restricted to Toulal or Beni Tajite ore deposits (Fig. 13). This could be due to sampling, but such rare occurrences may be explained by their particular physico-chemical conditions of formation or their habitus, since the thin encrustations could have been removed by erosion.

- Calcite occurrences of each ore deposit share common macroscopic and microscopic characteristics. Massive white calcite cleaving into rhombs was observed in each protore (Fig. 13) and may present evidence of deformation, identically to galena (Fig. 9B). At Toulal, white calcite fills the extrados fractures of the folds and is probably contemporaneous with folding. These early generations of white calcite must not be mistaken for the late generation of drusy translucent calcite, which cements the calamine breccia or fills the karst cavities (Figs. 5D and 6D).

- Internal sedimentation and recycling of ore is a continuous process during the development of the karst. At Tadaghast, sediments including quartz needles fragments fill the fractures of

the sphalerite lenses and predate the concretions of smithsonite (Fig. 10J). Conversely, in other deposits, internal sediments usually fill post-red calamine cavities. The occurrence of clayey materials like sauconite remains a constant, though (Fig. 13).

Evaluating the duration of mineral deposition is very subjective and may locally vary. In addition, genetic processes, like in situ replacement or distal precipitation, are not taken into account. Therefore, the above paragenetic successions need to be supplemented by a time-integrated holistic model, which best explains the evolution of the Moroccan High Atlas ore deposits (Section 6.2). Tectonics has also played a major role, and therefore it is crucial to integrate our model into the general evolution of the Moroccan High Atlas (Section 6.3).

### 6.2 General evolution of the Moroccan High Atlas non-sulfide zinc ore deposits

Although paragenetic sequences only provide an idealistic view of the ore evolution, they allow us to distinguish three types of ores (protore, red calamine, grey calamine) that correspond to three successive stages of the ore deposition. This evolution of the Moroccan supergene non-sulfide Zn ore deposits is not very different from that presented by Reichert and Borg (2008) for Iran. After protore accumulation, two successive stages of the supergene process are distinguished leading to the accumulation of two different types of calamine. However, the paragenesis may locally differ across ore deposits. For example, in Morocco, hemimorphite only occurs at the end of the second stage, whereas this phase is common during the whole supergene process in Iran. In addition, we have observed that hemimorphite always precipitates after hydrozincite, whereas Iranian non-sulfide Zn ore deposits are characterized by the reverse transition (Reichert et al., 2003). Conversely, our scenario is partly comparable to that described by Takahashi (1960) for American non-sulfides Zn ore

deposits. The strong variability of these evolutionary models reveals the sensitivity of each supergene non-sulfide ore deposit system to the physico-chemical modification, the tectonic setting and the climate environment. The following presents each stage of this evolution and includes 1) geochemical constraints, 2) spatial variability and 3) chemical and geometric relationships between the ore and the host material.

### 6.2.1 Pre-oxidation stage

As previously described, there is a strong lithological control of the protore deposition, which only occurs within limestone layers (Fig. 14A). The primary sulfides are galena, sphalerite and pyrite with various proportions and they appear as oblate horizons in concordance with the bedding of the host layer. Sphalerite is poor in Fe, and the Bi content of galena is consistent with the values reported by Mouguina (2004) for other sulfide deposits of the Moroccan High Atlas. Sulfides are closely associated with white massive calcite, which experienced a similar post-depositional deformation. Limestone formed in a reef environment contains a rich fauna of Upper Sinemurian (192-189 Ma) to Pliensbachian (189-183 Ma) corals (Leblanc, 1968; du Dresnay, 1979). Although the exact age of mineralization remains unknown, no rocks older than Mid-Liassic enclose ores with the aforementioned characteristics (Mouguina, 2004). Deposition of primary sulfides may closely follow the limestone sedimentation, although the hypothesis of epigenetic sulphide mineralization in selective strata cannot be ruled out.

Evidence of silicification was not observed in the field, but microscope observation has shown repeated occurences of small quartz needles persisting during the mineralization evolution (Fig. 14A). Bazin (1968) and Leblanc (1968) have described such events, which are also characterized by dissemination and impregnation of the limestone. Contrary to

silicification, dolomitization was minor in the studied ore deposits (Fig. 13) and limited evidence was only found at Toulal (Fig. 7A). Leblanc (1968) identified a network of pinkish-dolomite fractures that crosscut the stratification; but the link between the dolomite-rich zone and the ore body remains unknown. In the Bou Dahar massif, near Beni Tajite, Adil et al. (2004) advanced a partial replacement of the Liassic limestone hosting the mineralization by dolomite, although Agard and du Dresnay (1965) highlight its rarity. The lack of dolomite questions the origin of the protore. In comparison with the Touissit district (Wadjinny, 1989), the Pb-Zn ore deposits of High Atlas are usually considered as Mississippi Valley Type (MVT) (Bouabdellah et al., 2002; Adil et al., 2004; Mouguina and Daoudi, 2008). But, dolomitic rocks are remarkably rare and the scarcity of fluid inclusions constraint presently precludes a certain attribution to a given class of MVT. The relative absence of dolomite also suggests that its role for the calamine formation is limited to particular cases (Boni et al., 2011a).

### 6.2.2 Supergene stage I

In all studied deposits, limestone layers experienced compression related to the Atlas event and were folded. Locally, white calcite veins owing their origin to this folding episode were emplaced prior to the supergene alteration of the protore and the formation of calamines (Fig. 14B). Folding contributes to tilting of the strata until reaching the upright positions that facilitate the percolation of meteoric water. The mildly acid meteoric water infiltrates and dissolves the host limestone (Fig. 14B), giving rise to a large karst throughout the Jurassic formation of the Moroccan High Atlas (Combe et al., 1969; Couvreur, 1988; Bouchaou et al., 1997). When percolating water reaches the primary sulfides, $O_2$ also reacts with pyrite and simultaneously produce $Fe^{2+}$, $Fe^{3+}$, $Fe_2(SO_4)_3$, and $H^+$ (2, fig. 14B), leading to a decrease of

the pH (Herbert, 1999; Domènech et al., 2002). However, acidity is buffered by the dissolution of the host limestone (Descostes et al., 2002). Iron ions remain mostly trapped and precipitate to form iron oxi-hydroxide full pseudomorphs after pyrite. In addition, dissolved pyrite exposes a radial distribution of fractures (Fig. 7C), which indicates a continuous evacuation of sulfate anions (Kosakevitch, 1983). Such open system and the carbonate host rocks as well may have hindered the localization of general hyperacid environment and therefore the precipitation of ultralow pH minerals (e.g. jarosite) as classically observed in non-carbonate hosted sulfide ore deposits (Alpers et al., 1992). Precipitation of gypsum is classically advanced to explain the fate of sulfate anions (Huminicki, 2006; Reichert and Borg, 2008), but gypsum was rarely observed or described in Morocco. It is therefore crucial to consider a dynamic environment where most of the sulfate ions are removed from the karst system. Full pseudomorphs also attest to a slow oxidation process (Kosakevitch, 1983), which coincides with the formation of disordered hydrous materials like ferrhydrite. Under neutralized pH conditions, hematite and even lepidocrocite may precipitate (Bingham and Murad, 1997; Cornell and Schwertmann, 2003; Jönsson et al., 2006), whereas goethite only forms the external rim under early acidic conditions.

Neutralization in the karst environment is classically explained by the reaction between calcite (or dolomite) and $H^+$ (3, fig. 14B), which produces $H_2CO_3$ or $HCO_2^-$ (Huminicki and Rimstidt, 2008) depending on the local pH conditions. These dissolved phases can degas $CO_2$ until reaching equilibrium with pore gases in the vadose zone. As discussed by Reichert and Borg (2008), multiple mechanisms like transport in solution or diffusion can lead to a high partial pressure of $(CO_2)_g$, which facilitates the precipitation of secondary carbonates, like smithsonite (Brugger et al., 2003). Reaction involving organic matter (1, fig. 14B) is also a possible way to generate high $P(CO_2)_g$ (e.g. Boni et al., 2003),

but the arid climate of Morocco over the last tens of Myrs (Maley, 1980; Le Houérou, 1997) does not support a major role for organic matter degradation.

Oxidation also affects the other sulfides, which are variably dissolved under oxidizing conditions (Steger and Desjardins, 1980; Zeman, 1985; Nordstrom and Alpers, 1999). Galena and sphalerite preferably react with oxidation products of the pyrite dissolution like $Fe_2(SO_4)_3$ (4, fig. 14B). Consequently, $Pb^{2+}$ and $Zn^{2+}$ ions are released in the solution and they may combine with carbonate or sulfate ions. The formation of smithsonite, cerussite and anglesite is controlled by several physico-chemical parameters, such as pH, $(CO_2)_g$, or the concentration and the mobility of Zn and Pb species in solution. Details may be found in Takahashi (1960), Sangameshwar and Barnes (1983) and Ingwersen (1990). Under slightly acid pH and high $P(CO_2)_g$ conditions, carbonates can precipitate. Because of their high mobility, Zn ions may be transported over a long distance and, thus, smithsonite is found in every part of the ore body, including speleothemes. Conversely, Pb ions are less mobile and cerussite (type I cerussite) only occurs as rims around galena (5, fig. 14B). Since cerussite is almost insoluble in non-acid water (Garrels, 1954), such coating, known as armoring effect (Reichert and Borg, 2008) explains the ability of galena to resist in extreme altered profiles, like at Tizi n'Firest (Bazin, 1968). When $P(CO_2)_g$ or pH are abnormally low, anglesite can occur (Takahashi, 1960). In the Toulal ore, anglesite has been identified close to dissolved pyrite isolated within galena (Fig. 7D). As seen previously, pyrite oxidation is accompanied by an evacuation of sulfate ions out of the pseudomorphs, leading to a local increase of sulfate activity. In addition, cerussite that armors the galena limits buffering spatially and temporarily (Reichert and Borg, 2008). Consequently, the interface between pseudomorphing galena and pyrite represents a microenvironment with high activities of sulfate ions co-existing with moderate activities of carbonic acid under a pH below 6, which may have facilitated a

simultaneous precipitation of anglesite and cerussite around galena (Sangameshwar and Barnes, 1983).

Supergene secondary sulfides are common in calamine ores from each deposit. Covellite may occur as disseminated in the cerussite coating the galena of the protore. Secondary galena, covellite and probable greenockite often rim sphalerite relics in the course of being transformed into smithsonite (Figs. 7E, 10M and 10N). Such textures have been described in several other Zn ore deposits, in Ireland (Morrissey, 1970), in Zambia (Taylor, 1958; Terracciano, 2008) or in Namibia (Borg et al., 2003). The occurrence of aqueous lead is due to the oxidation of galena. Although primary Cu-bearing sulfides have not been observed in the samples, veins of chalcopyrite replaced by malachite are described in the Bou Dahar (Agard and du Dresnay, 1965) and in the Bou Arhous (Leblanc, 1968). Cd is an essential component of sphalerite, especially in carbonate host-rocks environment (Ivanov, 1964). When dissolved, sphalerite, which contains average amounts of Cd up to ca. 0.5% (Table 1), may have released Cd in the water. Formation of secondary Cu, Pb and Cd sulfides (6, fig. 14B) coating primary galena or sphalerite can be compared to the activation stage during flotation (Finkelstein, 1997), by copper ions (Pattrick et al., 1999), lead ions (Trahar et al., 1997) or cadmium ions (Ralston and Healy, 1980). The local variations of the level of the water table due to seasonal or tectonic effects may be responsible for short intervals of reducing conditions that facilitate the precipitation of supergene secondary sulfides. Reduction of sulfate ions by bacteria was also proposed to explain the secondary sulfides at Tynagh, Ireland (Sangameshwar and Barnes, 1983), but presently it is difficult to check this option in the case of the Moroccan Zn non-sulfide deposits.

Willemite occurs at Bou Arhous (Guillaume and Gaudrefroy, 1959; Leblanc, 1968), but its origin remains unexplained. Willemite directly replaces sphalerite and is associated with remnant galena and cerussite. This “black calamine” is always enclosed in clayey

material or surrounded by late hydrozincite. Willemite is traditionally considered of hydrothermal origin (Hitzmann et al., 2003) and mostly forms at high temperatures (Roy and Mumpton, 1956, Ingwersen, 1990; Brugger et al., 2003). Remarkable paradigms of such ore deposits are Franklin in USA (Frondel and Baum, 1974), Beltana in Australia (Grove et al., 2003), and Berg Aukas in Namibia (Cairncross, 1997; Boni et al., 2011b). However, the Bou Arhous ore deposit bears structural and paragenetic characteristics (e.g. absence of hydothermal veins, karstic network with conduits, association of willemite, carbonate and sauconite) that differ from hypogene mineralization. Similarly, non-sulfide Zn ore deposits of Belgium are dominated by willemite (Dejonghe et al., 1998), which hosts fluid inclusions supporting formation temperatures below 70°C (Coppola et al., 2008). Hypotheses like low-temperature hydrothermalism or specific conditions of oxidation have been advanced. Thermodynamic studies (Takahashi, 1960; Brugger et al., 2003) have demonstrated that, at surface temperature (ca. 25°C), willemite is stable under low water activities, alkaline pH, and oxidizing conditions. High silica activities accompanied by low $P(CO_2)_g$ are also necessary to precipitate silicate instead of carbonate (7, fig. 14B). Such specific environment occurs under arid supergene conditions (Pough, 1941; Markham, 1960), which facilitate high silica contents in waters. At Bou Arhous, extremely arid conditions have been recorded during the last tens of millions years like in other places of northern Africa (Maley, 1980). In addition, the occurrence of Triassic red clays and silicified limestone as well (Leblanc, 1968) may explain the prevalence of anhydrous zinc silicate.

### 6.2.3 Supergene stage II

This second stage of the supergene evolution is dominated by “grey to white calamine” and occurs after the partial to total consumption of pyrite due to oxidation, as

proposed by Reichert and Borg (2008). Consequently, $H^+$ ions are no longer released in the system and the pH conditions clearly become neutral to slightly alkaline. Buffering continues but is minor, and it is only due to the dissolution of the host limestone by the mildly acid meteoric water. The cessation of pyrite oxidation also influences the activity of the sulfate ions, which dramatically decreases. Hence, anglesite formed during the first stage may be dissolved and a secondary generation of cerussite (type II cerussite) precipitates. In situ replacement occurs in the galena crusts (Fig. 11D), but Pb ions can migrate over a short distance and precipitate in the rock cavities (Fig. 8H).

During this second stage, iron oxi-hydroxides, mainly goethite, still precipitates, with formation of botryoidal masses in the druses. The grey and white calamines are also dominated by smithsonite (Fig. 14C), which forms botryoidal crusts around the red calamines or fills cavities with euhedral crystals showing centripetal growth. Smithsonite incorporates diverse impurities dissolved in the water, like Fe that concentrates as growth bands. Under generalized neutral pH conditions, the precipitation of smithsonite causes a drop of $P(CO_2)_g$ that is no longer buffered. Under low partial pressure in carbon dioxide and arid conditions (Takahashi, 1960; McPhail et al., 2003), smithsonite can be replaced by hydrozincite (8, fig. 14C), which precipitates to form botryoidal masses. Replacement of smithsonite by hydrozincite produces carbon dioxide (Takahashi, 1960); this may explain why late smithsonite can also occur after hydrozincite stage (Fig. 13).

Contemporaneously to the precipitation of late goethite, descloizite and botryoidal encrustations of Mn-oxides occur and coat the red calamines ore (9, fig. 14C). Descloizite is an occasional mineral of Pb-Zn ore deposits, and was described for example at Goodsprings (Takahashi, 1960), Berg Aukas (Markham, 1960) and in other places in Namibia or Zambia (Boni et al., 2007; Kamona and Friedrich, 2007; Terracciano, 2008). To explain the formation of descloizite, Takahashi (1960) advanced the necessity of high V concentration and arid

climate. Oxidizing conditions also contribute to generate pentavalent vanadium that is able to combine with $Zn^{2+}$ and $Pb^{2+}$ to form descloizite. Boni et al. (2007) similarly suggest that descloizite can form when low pH and Eh conditions prevail. These authors identified V sources, such as silicoclastic and mafic rocks, and V was transported as calcium vanadate (Verwoerd, 1957). In Morocco, the source of V is unknown even in the Pb deposit of Mibladen (Jébrak et al., 1998) that contains a significant amount of vanadinite. The past arid climate is highly favorable to the formation of desclozite, especially in low Eh domains like the boundary between the vadose and phreatic zones (Boni et al., 2007). Pb-Zn bearing Mn oxides, like psilomelane (possibly coronadite and chalcophanite) are typical of supergene environments (Hewett, 1971). In studied ore deposits, the origin of Mn is unknown, although Mn ore deposits are widespread in northern Africa, like Imini in Southern Central High Atlas (Force et al., 1986), Bou Arfa in Eastern High Atlas (Bouladon and Jouravsky, 1956), or Tamra in Northwestern Tunisia (Decrée et al., 2010). Generally, Mn is transported as $Mn^{2+}$ and further oxidized to $Mn^{4+}$, when pH becomes neutral in high oxidizing conditions (Brookins, 1988). Hence, Mn-oxides can precipitate and incorporate aqueous iron, lead and zinc.

Botryoidal masses of hemimorphite have been repeatedly observed in all studied ore deposits. They always occur during the late stage of mineralization (10, fig. 14C). Hemimorphite crystals are well developed and their growth may resemble speleothemes, with a unipolar distribution in the cavities (Fig. 8I). Formation of hemimorphite during the supergene evolution is a debated issue, since the thermodynamic constraints are not available. In case of solutions saturated with silica, Takahashi (1960) and McPhail et al. (2003; 2006) proposed that hemimorphite is stable under pH below 7-8, for a given Zn concentration. The stability fields of hemimorphite and hydrozincite are overlapping, though. Hence, small variations of $P(CO_2)_g$, pH or Zn concentration may rapidly change the equilibrium of the

system, resulting in hemimorphite-hydrozincite assemblages (Reichert and Borg, 2008). Contrary to the Zn non-sulfide deposits in Iran, hemimorphite always occurs after hydrozincite in the studied sites of Moroccan calamines, suggesting a drop of the aforementioned physico-chemical parameters. This may be caused by the significant reduction of buffering owing to host limestone dissolution.

Internal sedimentation occurs throughout the development of the karst network and the process of supergene oxidation. However, much of the internal sediments were deposited lately, and they fill cavities of the gangue and the calamine as well (11, fig. 14C). Sauconite mainly composes the infilling material, although its origin is unclear. Sauconite is common in case of deposits emplaced in siliciclastic environments (Hitzman et al., 2003). Typical examples are Accha in Peru (Boni et al., 2009) or Skorpion in Namibia (Borg et al., 2003), where sauconite progressively replaces the dissolved feldspars or the micas of the gangue under arid conditions. Minor transport may also occur with distal deposition of the clays in karst cavities. Boni et al. (2009) also reported that, in certain cases, sauconite can replace hemimorphite during an early diagenetic stage, but corresponding textures were not observed in the Moroccan calamines. As impure limestone hosts the ore deposits, barren clays localized at site of styloliths can incorporate Zn and Mg, whereas Al and Si are partly removed (Terranciano, 2008). In Morocco, the Lower Jurassic series mainly display massive limestone, but interbedded marls and shale are quite common. As the karst has formed, these Al-Si rich strata have experienced mineral transformation instead of total dissolution. During their accumulation in karst cavities, the neo-formed clays could have reacted with the Zn cations of the solution to form sauconite. The coexistence of barren and Zn-bearing clays may indicate different stages of the karst evolution.

### 6.3 Relative chronology and integration in the High Atlas tectonic framework

During Mesozoic (Fig. 15A), the opening of the Atlantic Ocean and the Tethys has resulted in rifting across the Paleozoic terrains (Laville and Piqué, 1991). Normal faults reactivating Variscan structures contributed to the formation of horsts and grabens, which were rapidly transgressed (du Dresnay, 1988; Piqué, 1994). Carbonate platforms developed in shallow domains during the Early Jurassic, and reef limestone laterally graded into slope and deep-sea facies. Zn-Pb sulfides lenses emplaced throughout the future High Atlas domain afterwards. Age of this mineralization is not well constrained, but it is generally assumed to closely follow sedimentation and therefore to be Sinemurian to Pliensbachian (Mouguina, 2004). These deposits are mainly concordant with the bedding of the host rock, which often consists in para-reefal or reefal limestone (Leblanc, 1968). The ENE-WSW trending normal faults probably could have played a role of conduits to drive Zn-Pb rich solutions from depth to surface (Mouguina, 2004), although the hypothesis of intrabasinal flows can not be ruled out. Although, contemporaneous magmatism is locally recorded, its direct influence on the mineralization event is not established (Caïa, 1968). Sedimentation continued during Jurassic and Cretaceous until filling of the basin and inversion tectonics.

Since mid-Eocene (Fig. 15B), the area has recorded compressive tectonics, leading to the formation of the High Atlas fold-and-thrust belt (Frizon de la Motte et al., 2000, 2009). Inversion tectonics affected the Liassic normal faults, which were reactivated as thrusts (Teixell et al., 2003). These structures have controlled the localization of narrow anticlines characterized by highly deformed Triassic shale and gypsum in the core and Liassic strata that dip vertical. Alternatively, tilting was limited or not visible at Tadaghast and Beni Tajite.

During Tertiary and Quaternary periods (Fig. 15C), the combined effect of regional uplift and erosion contributed to exhume the Liassic strata and the hosted Zn-Pb sulfides. When the water table has fallen below the sulfides of protore, their supergene oxidation may

have started; it was accompanied by the simultaneous extension of the karst network in the Jurassic formations. The accurate age of the supergene mineralization is not established yet and further studies should be envisaged. The upright position of the sulfide lenses was certainly favorable for the percolation of the meteoric water and the subsequent formation of non-sulfide Zn ore deposits. In case of Tadaghast and Beni Tajite, vertical fractures were potential drains for the meteoric water and have caused an in situ replacement of the sub-horizontal sulfides lenses similar to the processes described more generally by Borg (2009). Infilling of these vertical fractures also occurred, either as internal sedimentation of the karst or as precipitation from a Zn-rich solution near the protore (ca. 10 m). The preservation of the Moroccan ore deposits suggests that erosion and uplift have remained limited in the area. This can be explained by the fact that the Atlasic compression was not a single continuous event, but rather corresponded to successive shortening episodes, which alternated with long periods of tectonic quiescence (Frizon de Lamotte et al., 2000, 2009). Although short wet episodes have potentially initiated the genesis of supergene non-sulfide Zn ore deposits, the mostly arid climate of Tertiary (Maley, 1980) can also account for the limited extent of erosion.

## 7) Conclusion

Understanding the formation of non-sulfide zinc ore deposits requires an integration of numerous geochemical, climatic and tectonic features. In addition, the local variations of the physico-chemical conditions at microscale and the original geometry of the protore may be the cause of the substantial differences between the ore deposits. It is therefore necessary to have a multi-scale approach on the non-sulfide zinc ore deposits to get a comprehensive view of their genesis.

This article presents the first modern study on the Moroccan supergene non-sulfide Zn ore deposits, which have been the focus of a renewed interest for commercial purposes and societal reasons. The detailed identification of minerals and their textures by different effective techniques has revealed a two-stage supergene evolution controlled by both climate and tectonics. Such external factors directly influence the level of the water table and the development of the karstic network. Consequently, non-sulfide Zn ore deposits that originate from stratiform sulfide lenses have been formed either by sulfide replacement or by infilling of karst conduits due to precipitation or internal sedimentation. This suggests that different formation processes may coexist in a given ore deposit, and as pointed out by Borg (2003) and Daliran et al. (2009), the classical nomenclatures of non-sulfide Zn ore deposits by Large (2001) or Hitzman et al. (2003) are probably too simplistic.

Although the six studied ore deposits present a similar first-order geochemical evolution, we have observed small discrepancies between these sites owing to various local and external factors. Climate conditions were generally similar in High Atlas, but studied zones have experienced differential deformation, as raised by their variable structural features. This has a direct influence on the amount of uplift and the local erosion of the strata, and it also controls the water table level and the ability to concentrate zinc metals in carbonate, silicate and hydrated equivalents. At the scale of Northern Africa, the Atlasic tectonics display heterochronous deformation episodes and lateral variations of the uplift and the tectonic style (e.g. Frizon de la Motte et al., 2000, 2009; Arboleya et al., 2004). The large Zn-Pb province of Northern Africa overlaps the area that experienced deformation related to the well-constrained Atlasic events (Rouvier et al., 1985). Therefore, a regional study of the supergene non-sulfide Zn ore deposits of Morocco, Algeria and Tunisia could help to better understand the relationships between the Altas tectonics and the supergene evolution of sulfide ore deposits.

Acknowledgements

This study benefited from a grant in the frame of the CALAMINES project supported by the Région Centre. Fieldwork has been financed by Managem. Many thanks are due to L. El Hassani and O. Baha for field support and for providing access to the different mines. We are also indebted to F. Foucher (CBM), I. Di Carlo (ISTO), P. Penhoud (ISTO), J.-G. Badin (ISTO) and S. Janiec (ISTO) for sample preparation, assistance for analyses and data treatment. We also express our gratitude to Franco Pirajno, Gregor Borg and an anonymous reviewer for their comments that significantly improve the manuscript.

References

Adil S, Bouabdellah M, Grandia F, Cardellach E, Canals A. Caractérisation géochimique des fluides associés aux minéralisations Pb-Zn de Bou-Dahar (Maroc). C R Geoscience. 2004;336:1265-72. French.

Agard J, du Dresnay R. La région minéralisée du Jbel Bou-Dahar, près de Beni Tajjit (Haut Atlas oriental) : Étude géologique et métallogénique. Notes Mém Serv Géol Maroc, Rabat. 1965;181:135-66. French.

Alpers CN, Rye RO, Nordstrom DK, White LD, Bi-Shia K. Chemical, crystallographic and stable isotope properties of alunite and jarosite from acid-hypersaline Australian lakes. Chem Geol. 1992;96:203-26.

Andrew-Jones DA. The Application of Geochemical Techniques to Mineral Exploration. Collorado Sch Mines-Mineral Indust Bull. 1968;11:1-31.

Arboleya ML, Teixell A, Charroud M, Julivert M. A structural transect through the High and Middle Atlas of Morocco. J Afr Earth Sci. 2004;39:319-27.

Auajjar J, Boulègue J. Les minéralisations Pb-Zn (Cu) Ba du socle paléozoïque et de la plate-forme liasique du district du Tazekka (Taza, Maroc oriental): une synthèse. Chron Rech Min. 1999;536-537:121-35. French.

Bazin D. Etude géologique et métallogénique des chaînons atlasique du Tizi n'Firest au Nord de Ksar-es-Souk, Maroc. Notes Mém Serv Géol Maroc, Rabat. 1968;206:37-114. French.

Beauchamp W, Allmendinger RW, Barazangi M, Demnati A, El Alji M, Dahmani M. Inversion tectonics and the evolution of the High Atlas Mountains, Morocco, based on a geological-geophysical transect. Tectonics. 1999;18:163-84.

Bigham JM, Murad E. Mineralogy of ochre deposits formed by the oxidation of iron sulfide minerals. Adv Geo Ecol. 1997;30:193-225.

Bladh KW, 1982 : The Formation of Goethite, Jarosite, and Alunite during the Weathering of Sulfide-Bearing Felsic Rocks. Econ Geol. 1934;77:176-84.

Blanchard R, Boswell PF. Additionnal limonite types of galena and sphalerite derivation, Econ Geol. 1934;29:671-690.

Boni M, Gilg HA, Aversa G, Balassone G. The "Calamine" of SW Sardinia (Italy): geology, mineralogy and stable isotope geochemistry of a supergene Zn-mineralization. Econ Geol. 2003;98:731-748

Boni M, Balassone G, Arseneau V, Schmidt P. The nonsulfide zinc deposit at Accha (Southern Peru): geological and mineralogical characterization. Econ Geol. 2009;104:267-89.

Boni M, Large DE. Nonsulfide zinc mineralization in Europe: An overview. Econ Geol. 2003;98:715-729.

Boni M, Mondillo N, Balassone G. Zincian dolomite: A peculiar dedolomitization case? Geology. 2011a;39:183-6.

Boni M, Terracciano, Balassone Gleeson SA, Matthews AH. The carbonate-hosted willemite prospects of the Zambezi Metamorphic Belt (Zambia). Min Depos. 2011b;46:707-29.

Boni M, Terracciano, Evans N, Laukamp C, Schneider J, Bechstädt T. Genesis of vanadium ores in the Otavi Mountainland (Namibia). Econ Geol. 2007;102:441-69.

Borg G. Geological and economical significance of supergene nonsulphide zinc deposits in Iran and their exploration potential. In: 20th World Mining Congress, Tehran;2005, p. 385-390.

Borg G. Surface-related formation, upgrading, and improvement of ore deposits – A review of supergene metallogenic processes. In: Eliopoulos DG et al., editors. Mineral Exploration and Sustainable Development. Millpress;2003. p. 61-64.

Borg G. The role of fault structures and deep oxidation in supergene base metal deposits. In: Titley SR, editor. Supergen environments, processes and products. Econ Geol Sp Publ 14; 2009. p. 121-132.

Borg G, Kärner K, Buxton M, Armstrong R, Schalk van der Merve W. Geology of the Skorpion non-sulphide deposit, southern Namibia. Econ Geol. 2003;98:749-71.

Bouabdellah M, Boudchiche L, Ouahhabi B, Baba M, Naciri T. Les minéralisations plombo-zincifères de Bou-Dahar (Haut Atlas oriental) : un exemple de minéralisation de type Mississippi Valley. In: 19e Colloq Afr Géol, Maroc; 2002. p. 37. French.

Bouchaou L, Chauve P, Mudry J, Mania J, Hsissou Y. Structure et fonctionnement d'un hydrosystéme karstique de montagne sous climat semi-aride: cas de l'Atlas de Beni Mellal (Maroc). J Afr Earth Sci. 1997;25:225-36. French.

Bouladon J, Jouravsky G. Les gîtes de manganese du Maroc. In: Manganeso 2. Mexico;1956. p. 217-48. French.

Brechbühler YA, Bernasconi R, Schaer JP, Jurassic sediments of the Central High Atlas of Morocco: deposition, burial and erosion history. In: Jacobshagen V, editor. The Atlas system of Morocco: Lect Notes Earth Sci 15;1988. p. 139-68.

Brookins DG. Eh-pH diagrams for geochemistry. New York: Springer-Verlag; 1988.

Brugger J, McPhail DC, Wallace M, Waters J. Formation of willemite in hydrothermal environments. Economic Geology. 2003;98:819-35

Bruyere D, De Putter T, Decree S, Dupuis C, Fuchs Y, Jamoussi F, et al. Miocene karsts and associated Fe–Zn-rich minerals in Aïn Khamouda (Central Tunisia). J Afr Earth Sci. 2010;57:70-8.

Bustamante H, Shergold HL. Surface chemistry and flotation of zinc oxide minerals. Institution of mining and metallurgy. 1983;92:C201-8.

Caïa J. Roches eruptives básiques et minéralisations en plomb, zinc et strontium de la region de Tirrhist (Haute Atlas de Midelt). Notes Mem Serv Geol Maroc 1968;206:7-30. French.

Cairncross B. The Otavi Mountain Land Cu-Pb-Zn-V deposits. Mineralogical Record. 1997; 28:109-30.

Charrière A, Haddoumi H, Mojon PO. Deécouverte de Jurassique supérieur et d'un niveau marin du Barrémien dans les "couches rouges" continentales du Haut Atlas central marocain : implications paléogéographiques et structurales. C R Palevol. 2005;4:385-94. French.

Charrière A, Haddoumi H, Mojon PO. Ferrière J, Cuche D, Zili L. Mise en évidence par charophytes et ostracodes de l'âge paléocène des dépôts discordants sur les rides anticlinales de la région d'Imilchil (Haut Atlas, Maroc): conséquences paléo-géographiques et structurales. C R Palevol. 2009;8:9-19. French.

Cheddadi R, Lamb HF, Guiot J, van der Kaars S. Holocene climatic change in Morocco: a quantitative reconstruction from pollen data. Climate Dynamics. 1998;14:883-90.

Chèvremont P. Les roches éruptives basiques des boutonnières de Tassent et Tasraft et leurs indices métallifères dans leur cadre géologique (Haut Atlas central, Maroc) [dissertation]. Lyon: Université Claude Bernard; 1975. French.

Chukhrov FV. Hypergene iron oxides in geological processes. Moscow: Nauka; 1975. Russian.

Cole PM, Sole KC. Solvent extraction in the primary and secondary processing of zinc. J South Afr Inst Min Metall. 2002;102:451-6.

Combe M, Hazan R, Moniton L, Thauvin J-P. Bibliographie hydrogéologique analytique du Maroc 1958-1968. Rabat: Editions du Service géologique du Maroc; 1969. French.

Coppola V, Boni M, Gilg HA, Balassone G, Dejonghe L. The "calamine" nonsulfide Zn–Pb deposits of Belgium: petrographical, mineralogical and geochemical characterization. Ore Geol Rev. 2008;33:187-210.

Cornell RM, Schwertmann U. The Iron Oxides: Structure, Properties, Reactions, Occurrence and Uses, second, completely revised and extended. Weinheim: Wiley-VCH Verlag GmbH & Co. KGaA; 2003.

Couvreur G. Essai sur l'évolution morphologique du Haut Atlas central calcaire (Maroc). Notes Mem Serv Geol Maroc. 1988; 318. French.

Dagallier G. Une série carbonatée littorale: le Lias moyen (à Pb-Ba) de Mibladen (Maroc): Dolomitisation et dissolution polyphasées en environnement tectonique semi-mobile. Sciences de la Terre. 1977; 21:53-101. French.

Daliran F, Borg G, Armstrong R, Walther J, Vennemann T, Friese K, et al. Nonsulphide Zinc Deposits, Iran – The Hypogene Emplacement and Supergene Modification History of the Angouran Zinc Deposit, NW-Iran. Berichte zur Lagerstätten und Rohstoffforschung, 57. Hannover: Bundesanstalt für Geowissenschaften und Rohstoffe; 2009. 75 p.

Decrée S, Marignac C, De Putter T, Deloule E, Liégeois J-P, Demaiffe D. Pb–Zn mineralizations in a Miocene regional extensional context: the case of the Sidi Driss and the Douahria ore deposits (Nefza mining district, N. Tunisia). Ore Geol Rev. 2008;34:285-303.

Decrée S, Ruffet G, De Putter T, Baele J-M, Recourt P, Jamoussi, et al. Mn oxides as efficient traps for metal pollutants in a polyphase low-temperature Pliocene environment: A case study in the Tamra iron mine, Nefza mining district, Tunisia. J Afr Earth Sci. 2010;57:249-61.

Dejonghe L, Zinc–lead deposits of Belgium. Ore Geol Rev. 1998;12:329-54.

Descostes M, Beaucaire C, Mercier F, Savoye S, Sow J, Zuddas P. Effect of carbonate ions on pyrite (FeS2) dissolution. Bull Soc Geol France. 2002;173:265-70.

Domènech C, De Pablo J, Ayora C. Oxidative dissolution of pyritic sludge from the Aznalcóllar mine (SW Spain). Chem Geol. 2002;190:339-53.

du Dresnay R. Sédiments jurassiques du domaine des chaînes atlasiques du Maroc. In Symposium “Sédimentation jurassique W européenne”. A.S.F. Pub Sp. 1979;345-365. French.

du Dresnay R. Recent data on the geology of the Middle Atlas (Morocco). In: Jacobshagen V, editor. The Atlas system of Morocco: Lect Notes Earth Sci. 1988;15:293-320.

Emberger A. Carte polygénétique des minéralisations plombifères de la Haute Moulouya (gisements d’Aouli, Mibladen et Zaida), Maroc. C R Acad Sci Paris. 1965;260: 3433-6. French.

Emberger A. Carte des minéralisations plombo-zincifères du Maroc map : gîtes et indices renfermant du plomb ou du zinc en élément majeur ou mineur [map]. Rabat: Service géologique du Maroc; 1969.

Emberger A. Méthodologie de la recherché métallogénique: la classification morpho-lithologique des minéralisations plombo-zincifère du Maroc. Notes Serv Geol Maroc. 1970;225:155-78. French.

Finkelstein NP. The activation of sulphide minerals for flotation: a review. Int J Mineral Process. 1997;52:120-81.

Force ER, Back W, Spiker EC, Knauth LP. A ground-water mixing model for the diagenesis of the Imini manganese deposit (Cretaceous) of Morocco. Econ Geol. 1986;81:65-79.

Frizon de Lamotte D, Leturmy P, Missenard Y, Khomsi S, Ruiz G, Saddiqi O, et al. Mesozoic and Cenozoic vertical movements in the Atlas system (Algeria, Morocco, Tunisia): An overview. Tectonophysics. 2009;475:9-28.

Frizon de Lamotte D, Saint Bezar B, Bracene E, Mercier E. The two main steps of the Atlas building and geodynamics of the western Mediterranean. Tectonics. 2000;19:740-61.

Frizon de Lamotte D, Zizi M, Missenard Y, Hafid M, El Azzouzi M, Charrière A, et al. The Atlas system. In : Michard A, Saddiqi O, Chalouan A, Frizon de Lamotte D, editors.

Continental Evolution: The Geology of Morocco. Structure, Stratigraphy, and Tectonics of the Africa-Atlantic-Mediterranean Triple Junction. Springer-Verlag; 2008. p. 133-202.

Frondel C, Baum JL. Structure and mineralogy of the Franklin zinc-iron-manganese deposit, New Jersey. Econ Geol. 1974;69:157-80.

Garrels RM. Mineral species as function of pH and oxidation potentials, with special reference to the zone of oxidation and secondary enrichment of sulfide ore deposits. Geoch Cosmoch Acta. 1954;5:158-9.

Gaudefroy C. Kaolinite et montmorillonite zincifères (sauconite?) d'Iboughalène. Notes Mém Serv Géol Maroc 1959;144:152-3. French.

Gnoinski J. Skorpion Zinc: optimization and innovation. J South Afr Inst Min Metall. 2007;107:657-62.

Gomez F, Allmendinger R, Barazangi M, Beauchamp W. Role of the Atlas Mountains (northwest Africa) within the African-Eurasian plate-boundary zone. Geology. 2000;28:775-8.

Groves I, Carman CE, Dunlap WJ. Geology of the Beltana Willemite Deposit, Flinders Ranges, South Australia. Econ Geol. 2003;98:797-818.

Guillaume C, Gaudefroy C. Dolomite de quelques gisements salifères du Maroc. Notes Serv Geol Maroc. 1959;144:129-47. French.

Haddoumi H, Charrière A, Andreu B, Mojon P-O. Les dépôts continentaux du Jurassique moyen au Crétacé inférieur dans le Haut-Atlas oriental (Maroc): Paléoenvironnements successifs et signification paléogéographique, Carnets de Géologie - Notebooks on Geology, Brest, 2008/XX (CG2008 AXX). http://paleopolis.rediris.es/cg/ French.

Herbert RB, 1999. Sulphide oxidation in mine waste deposits, a review with emphasis on dysoxic weathering.Mitigation of the environmental impact from mining waste (MiMi). MiMi Print, Luleå, Sweden

Herbig HG, Trappe J, Stratigraphy of the Subatlas Group (Maastrichtian-Middle Eocene, Morocco). Newsl Stratigr. 1994;30:125-65.

Heyl AV, Bozion CN. Oxidized zinc deposits of the United States, Part 1. General Geology: U.S. Geological Survey Bulletin. 1962;1135-A, 52 p.

Hewett DF. Coronadite; modes of occurrence and origin Econ Geol. 1971;66:164-77.

Hitzman MW, Reynolds NA, Sangster DF, Allen CR, Carman CE. Classification, Genesis, and Exploration Guides for Nonsulfide Zinc Deposits. Econ Geol. 2003;98:685-714.

Hosseini SH. Physicochemical studies of oxide zinc mineral flotation [dissertation]. Luleå: University of Technology; 2008.

Huminicki DMC. Effect of coatings on mineral reaction rates in acid mine drainage [dissertation]. Virginia Polytechnic Institute and State University; 2006.

Huminicki DMC, Rimstidt JD. Neutralization of sulfuric acid solutions by calcite dissolution and the application to anoxic limestone drain design. Appl Geochem. 2008;23:148-65.

Ingwersen G. Die sekundären Mineralbildungen der Pb–Zn– Cu–Lagerstätte Tsumeb, Namibia. [dissertation]. University Stuttgart; 1990. German.

Ivanov VV. 1964, Distribution of cadmium in ore deposits. Geokhimiya. 1964;4:757-68. Russian.

Jambor JL. Mineralogy of Sulfide-rich Tailings and Their Oxidation Products. In: Jambor JL, Blowes DW, editors. Environmental Geochemistry of Sulfide Mine-wastes. Mineralogical Association of Canada, Short Course 22; 1994.p. 59–102.

Jébrak M, Marcoux E, Masloubi M, Zaharaoui M. From sandstone- to carbonate-hosted stratabound deposits: an isotope study of galena in the Upper-Moulouya District (Morocco). Mineral Dep. 1998;33:406-15.

Jolivet L, Faccenna C. Mediterranean extension and the Africa-Eurasia collision. Tectonics. 2000;19:1095-106.

Jönsson J, Jönsson J, Lövgren L. Precipitation of secondary Fe(III) minerals from acid mine drainage. Appl Geochem 2006;21:437-45.

Kamona AF, Friedrich GH. Geology, mineralogy and stable isotope geochemistry of the Kabwe carbonate-hosted Pb-Zn deposit, central Zambia. Ore Geol Rev. 2007;30:217-243.

Kosakevitch A (Bureau des Ressources Géologiques et Minières). Etude morphogénétique des textures de remplacement et de remplissage dans les chapeaux de fer; 1983. Report No.: 83SGN936MGA.

Large D. The geology of non-sulphide zinc deposits - An overview. Erzmetall. 2001.vol. 54, p. 264-276.

Laville E, Piqué A. La distension crustale atlantique et atlasique au Maroc au début du Mésozoïque: le rejeu des structures hercyniennes. Bull Soc Geol Fr. 1991;162:1161-71.

Laville E, Piqué A. Jurassic penetrative deformation and Cenozoic uplift in the central High Atlas (Morocco): A tectonic model. Structural and orogenic inversions. Geol Rundsch. 1992;81:157-70.

Laville E, Piqué A, Amrhar M, Charroud M. A restatement of the Mesozoic Atlasic rifting (Morocco). J Afr Earth Sci. 2004;38:145-53.

Le Houérou HN. 1997. Climate, flora and fauna changes in the Sahara over the past 500 million years. J of Arid Environ. 1997;37:619-47

Leblanc M. Etude géologique et métallogénique du jbel Bou-Arhous et de son prolongement oriental (Haut Atlas marocian oriental). Notes Mém Serv Geol Maroc 1968;206:117-206. French.

Maley J. Les changements climatiques de la fin du Tertiaire en Afrique: leurs conséquences sur l'apparition du Sahara et de sa végétation. In: Williams AJ, Faure H, editors. The Sahara and the Nile, Rotterdam: Balkema; 1980. p. 63–86.

Markham NL, The willemite-hemimorphite relationship. Econ Geol. 1960;55:844-7.

Mattauer M, Tapponier P, Proust F, Sur les m´ecanismes de formation des chaînes intracontinentales. L'exemple des chaînes atlasiques du Maroc. Bull Soc Geol Fr. 1977;19:521-6.

McPhail DC, Summerhayes E, Jayaratne V, Christy A. Hemimorphite solubility and stability of low-T zinc minerals. In: V.M. Goldschmidt Conference 2006, ed. Conference Program Committee, Elsevier, United Kingdom, pp. A414.

McPhail DC, Summerhayes E, Welch S, Brugger J. The Geochemistry of Zinc in the Regolith. In: Roach IC, editor. Advances in Regolith. CRC for Landscape Environments and Mineral Exploration; 2003. p. 287–291.

Missenard Y, Cadoux A. Can Moroccan Atlas lithospheric thinning and volcanism be induced by Edge-driven Convection? Terra Nova. 2011;24:27-33.

Morrissey CJ. The mineralogy, structure and origin of the lead-zinc-copper residual ore body at Tynagh, Co., Galway, Ireland [dissertation]. Imperial College, London University Stuttgart; 1970.

Mouguina EM. Minéralisations polyphasées de couverture (Zn, Pb, Cu, Fe, As) liées au magmatisme d'un rift avorté au Jurassique. Région de Talmest-Tazoult : Haut Atlas central Maroc [dissertation]. Université de Tunis; 1992.

Mouguina EM. Les minéralisations polymétalliques (Zn-Pb, Cu, Co, Ni) du Jurassique du Haut Atlas central (Maroc): Contexte géodynamique, typologies et modèles génétiques [dissertation]. Faculté des Sciences Semlalia, Marrakech; 2004.

Mouguina EM, Daoudi L. Minéralisation Pb-Zn du type MVT de la région d'Ali ou Daoud (Haut Atlas Central, Maroc) : caractérisations du gîte et relations avec les cortèges de minéraux argileux. Estud Geol. 2008;64:135-50.

Mouguina EM, Bouabdelli M, Tlig S. Le gisement a Pb-Zn de Tazoult (Haut-Atlas central, Maroc); caracteres geologiques, mineralogiques et geochimiques; modele tectonique de mise en place. Chron Rech Min 1999;536-537:151-69. French.

Nordstrom DK, Alpers CN. Negative pH, efflorescent mineralogy, and consequences for environmental restoration at the Iron Mountain Superfund site, California. Proc Nat Acad Sci. 1999;96:3455-62.

Ovtracht A. Province plombo-zincifère du Haut Atlas central. Mines, Géologie et Energie, Rabat. 1978;44:103-9.

Pattrick RAD, England KER, Charnock JM, Mosselmans JFW. Copper activation of sphalerite and its reaction with xanthate in relation to flotation: an X-ray absorption spectroscopy (reflection extended X-ray absorption fine structure) investigation. Int J Mineral Process. 1999;55:247-65.

Piqué A, Géologie du Maroc, les domaines régionaux et leur évolution structurale. Marrakech: Pumag; 1994.

Piqué A, Michard A. Moroccan Hercynides: a synopsis. The Paleozoic sedimentary and tectonic evolution at the northern margin of West Africa. Am J Sci. 1989;289:286-330.

Popov A. Les types morphologiques et la répartition des gisements de zinc et de plomb en Algérie. Ann Min Geol, Tunis 1968;23:103-203.

Pough FH. Occurrence of willemite. Am Mineral. 1941;26:92-102.

Ralston J, Healy TW. Activation of zinc sulphide with Cu(II), Cd(II) and Pb(II) I: in weakly acidic media. Int J Mineral Process. 1980;7:175-201.

Ramdohr P. The ore minerals and their intergrowth. Oxord: Pergamon Press; 1969.

Reichert J, Borg G. Numerical simulation and a geochemical model of supergene carbonate-hosted non-sulphide zinc deposits. Ore Geol Rev. 2008;33:134-51.

Reichert J, Borg G, Rashidi B. Mineralogy of Calamine Ore from the Mehdi Abad Zinc–Lead Deposit, Central Iran. In: Eliopoulos DG, et al., editor. Mineral Exploration and Sustainable Development. Rotterdam: Millpress; 2003. p. 97-100.

Rognon P. Late quaternary climatic reconstruction for the Maghreb (North Africa) = Reconstitution climatique au Quaternaire supérieur du Maghreb (Afrique du Nord). Palaeogeography, palaeoclimatology. 1987;58:11-34.

Rouvier H, Perthuisot V, Mansouri A. Pb–Zn deposits and salt-bearing diapirs in Southern Europe and North Africa. Economic Geology. 1985;80:666-87.

Roy D, Mumpton NL. Stability of minerals in the system ZnOSiO2-H2O. Econ Geol. 1956;51:432-43.

Saddiqi O, El Haimer FZ, Michard A, Barbarand J, Ruiz GMH, Mansour EM, et al. Apatite fission-track analyses on basement granites from south-western Meseta, Morocco : Paleogeographic implications and interpretation of AFT age discrepancies. Tectonophysics. 2009;475:29-37.

Sangameshwar SR, Barnes HL. Supergene processes in zinc–lead–silver sulfides ores in carbonates. Econ Geol. 1983;78:1379-97.

Santoro L, Boni M, Herrington R, Clegg A. The Hakkari nonsulfide Zn-Pb deposit in the context of other nonsulfide Zn-Pb deposits in the Tethyan Metallogenetic Belt of Turkey, Ore Geol Rev. 2013; doi:10.1016/j.oregeorev.2013.01.011.

Scott KM, Ashley PM, Lawie DC. The geochemistry, mineralogy and maturity of gossans derived from volcanogenic Zn-Pb-Cu deposits of the eastern Lachlan Fold Belt, NSW, Australia, J Geochem Exp. 2001;72:169-91.

Smirnov SS. The Zone of Oxidation of Sulfide Ore Deposits. Leningrad: United Sci Tech Press; 1936.

Steger HF, Desjardins LE. Oxidation of sulfide minerals. V. Galena, sphalerite and chalcocite. Can Mineral. 1980;18:365-72.

Takahashi T. Supergene alteration of zinc and lead deposits in limestone. Econ Geol. 1960;55:1084-115.

Taylor JH. The formation of supergene galena at Broken Hill,northern Rhodesia. Mineral Mag. 1958;31:908-13.

Teixell A, Arboleya M-L, Julivert M, Charroud M. Tectonic shortening and topography of the central High Atlas (Morocco). Tectonics. 2003;22:1051. doi:10.1029/2002TC001460.

Terracciano R. Willemite mineralization in Namibia and Zambia [dissertation]. Università di Napoli; 2008.

Trahar WJ, Senior GD, Heyes GW, Creed MD. The activation of sphalerite by lead—a flotation perspective. Int J Mineral Process. 1997;49:121-48.

Verati C, Rapaille C, Féraud G, Marzoli A, Marzoli H, Bertrand H, et al. Ar-Ar ages and duration of the Central Atlantic magmatic province volcanism in Morocco and Portugal and its relation to the Triassic-Jurassic boundary. Paleogeogr Paleoclim Paleoecol 2007;244:308-25.

Verwoerd WJ. The mineralogy and genesis of the lead-zinc-vanadium deposit of Abenab West in the Otavi Mountains, south west Africa. Annals University of Stellenbosch. 1957;33:235-329.

Wadjinny A. Un panorama du district à plomb-zinc de Touissit, type de gisements stratoïdes en milieu carbonaté. Chron Rech Min. 1989;495:15-20.

Warme JE. Jurassic carbonate facies of the central and eastern High Atlas rift, Morocco. In: Jacobshagen V, editor. The Atlas system of Morocco: Lect Notes Earth Sci 15;1988. p. 169-99.

Zeman J. Supergene alteration of sulfides, II. A laboratory electrochemical study. Scripta Facultatis Scientiarum Naturalium Universitatis Purkynianae Brunensis, Geologia. 1985;15:115-36.

Figure captions

Figure 1 Simplified tectonic map of Western Mediterranean Sea and western North Africa, illustrating the relationships between High Atlas and the Alpine Belt (modified from Gomez et al., 2000). MA: Middle Atlas.

Figure 2 A: geological map of the Moroccan High Atlas. The location of the Pb-Zn prospects (white circle) and studied ore deposits (yellow star) is also indicated. B: cross-section of the Moroccan High Atlas, illustrating the structure of the fold-and-thrust belt and the connection between the Mesozoic cover and the Paleozoic basement (Modified after Teixell et al., 2003)

Figure 3 The Toulal prospect. A: simplified geologic map of the prospect area, showing the location of the macrostructures (C to G). B: schematic cross-section of the anticline, illustrating the superimposition of compression and collapse events (not to scale). C: view of the allochtonous Upper Sinemurian strata, which experienced syn-to post folding collapse accommodated by normal faults. D: structure of the periclinal termination, with microbreccia and cataclasite related to thrusting. E: syn-folding white calcite veins distributed in the extrados fractures of the anticline. F: aspect of the calamine network, forming N70°E-striking boudin-like veins. G: relation between tilted limestone strata and horizontal marl of internal sediments. In C, D, and G, thin (thick) strokes represent the trend of the bedding (fault)

Figure 4 The Bou Arhous ore deposit. A: geological map of the Jbel Bou Arhous, including the location of the Bou Arhous, Atchana and Iboughalene mines and the other Pb-Zn ore prospects (modified after Leblanc, 1968), B: cross-sections across the Jbel Bou Arhous, illustrating the lateral variations of the ramp anticline and the collapse structures. C: triassic purple clays along the “Grand Accident” thrust (G.A.) that parallels the anticlinal

axis of the Jbel Bou Arhous. D: hydrozincite coating bearing vertical-dipping lineation related to the “Grand Accident” thrust. E: squashed Triassic red clays with gypsum beds along the “Grand Accident” thrust. F: view of the southern flank of the Jbel Bou Arhous exposing cavities originally filled by calamine. G: view of the ore body including intricate patches of sulfide (galena) and white calcite rimmed by Zn-bearing carbonates and Fe-hydroxides. H: horizontal purplish marls, spotted with clasts of willemite and related to internal sedimentation within the karst cavities.

Figure 5 The Tadaghast ore deposit. A: sedimentary breccia within the Lower Jurassic limestone. B: internal sediments (marls) with subhorizontal bedding. C: N-S striking conjugate fault planes, showing en échelon veins of white calcite. D: cockade breccia with broken fragments of limestone cemented by banded calcite. E: oblique veins of massive white calcite intersected by a vertical rusty decimeter-scale banded calamine vein, F: profile of a mineralized horizon, showing the distribution of Zn (bottom) and Pb (top) sulfides and non-sulfides minerals. G: schematic 3D model of the Tadaghast ore deposit, illustrating the relations between lithologies and structures (see text for explanation). Letters refer to the aforementioned observations.

Figure 6 Other studied ore deposits of the Moroccan High Atlas. A: galena and translucent calcite separated from the host limestone by banded calcite (Beni Tajite ore deposit); this may represent an early karst stage contemporaneous to the sulfide mineralization. B: zoning within a calamine vein, with banded red smithsonite rimmed by white hydrozincite (Beni Tajite ore deposit). C: vertical veins filled by primary calcite, cross cut by red calamine afterward (Aït Labbes ore deposit). D: cockade breccia with fragments of red calamine cemented by calcite; the breccia is itself rimmed by radially banded calcite (Aït Labbes ore deposit).

Figure 7 The Toulal ore prospect, Part I. A: X-ray diffraction pattern of dolomitized limestone. B : inclusions of sphalerite and pyrite within galena rimmed by cerussite (RL, nic. //). C: iron oxi-hydroxides pseudomorph after pyrite, including dark grey ferrihydrite and grey goethite partly transformed into hematite (RL, nic. //). D : Raman composition map of the iron oxi-hydroxides pseudomorph after pyrite. Note the presence of anglesite associated with cerussite coating the galena (Black zone in the composition map). Anglesite was only observed close to pseudomorphed pyrite. Green for remnant carbon coating. E: covellite surrounding relics of sulfides within smithsonite (RL, nic. //). F: X-ray diffraction pattern of red calamine. Intensity (y axis) is normalized to the value of the higher peak. G : section of smithsonite rhombs, with growth banding revealed by a pigmentation of iron oxi-hydroxides (RL, nic. +). H: successive stages of smithsonite precipitation, cemented by calcite; early nodules of oxidized smithsonite (Sm I) are rimmed by a secondary smithsonite (Sm II), with variable iron oxi-hydroxides content (TL, nic. +). I and J : Zn and Fe X-ray composition maps of red calamine, respectively. A relative scale is given to the right with purple (red) corresponding to lowest (highest) element content. Black for no data. Abbreviations: Cc: calcite, Cer: cerussite, Chp: chalcophanite, Cor: coronadite, Cov: covellite, Dsc: descloizite, Fhd: ferrihydrite, Gal: galena, Goe: goethite, Grn : greenockite, Hem: hematite, Hmp: hemimorphite, Hdz: hydrozincite, Lpd: lepidocrocite, Py: pyrite, Qz : quartz, Sau : sauconite, Sm: smithsonite, Sph: sphalerite, Wlm : willemite. RL: reflected light, TL: transmitted light. Nic. // : Parallel nicols, Nic. + : Crossed nicols.

Figure 8 The Toulal prospect ore, Part II. A: iron oxi-hydroxides encrusting the smithsonite associated with descloizite and psilomelane aggregates, including coronadite and chalcophanite. Cavities are filled by Zn-rich clays and hydrozincite, whereas the final filling is made of hemimorphite and calcite (RL, nic. //), B: EDS spectrum and BSE

images of descloizite. Open dot represent the position of analysis. C: a psilomelane aggregate, with a botryoidal banded mixture of coronadite and chalcophanite (RL, nic. //). D: EDS spectrum and BSE image of a psilomelane aggregate. E: scalenohedral sections of smithsonite crystals encrusting the wall of a geode later filled by Zn-rich clays, with evidence of mud-cracking (TL, nic. //). F: X-ray diffraction pattern of clayey material within geodes, G: Hydrozincite impregnation of oxidized smithsonite (RL, nic. +). H: secondary cerussite filling geodes and postdating the formation of iron oxi-hydroxides (RL, nic. +). I: prismatic sections of hemimorphite crystals associated with calcite, which displays zoning possibly related to the growth bands of the original smithsonite crystals. Note that hemimorphite seems to have developed along a specific wall of the cavity (TL, nic. +). Abbreviations are given in fig. 7.

Figure 9 The Bou Arhous ore deposit. A: deformed galena associated with calcite (RL, nic. //). B: deformed crystals of calcite associated with galena (TL, nic. +). C: botryoidal cerussite coating galena (RL, nic. //). Note the "dusting" of galena in the cerussite rhythmic bands. D and E: X-ray diffraction patterns of black calamine. F: complex association of willemite and sulfides (galena and sphalerite). G: EDS spectrum and BSE image of willemite. H: relics of cerussite-galena aggregates and quartz needles cemented by an assemblage of willemite and smithsonite (RL, nic. //). Note that quartz needles are affected by microfractures and document microboudinage. I: EDS spectrum and BSE image of clayey material within geodes. The detailed image of clays was taken using SE imaging mode. J: radial nodules of hydrozincite and tabular sections of hemimorphite crystals filling cavities (TL, nic. +). Abbreviations are given in fig. 7.

Figure 10 The Tadaghast ore deposit. A: microphotograph of growth banded sphalerite (TL, nic. //). B and C: respective Fe and Cd X-ray composition maps of area presented in fig. 10A, illustrating that opaque bands correspond to higher content in Fe and Cd. D:

microphotograph of sphalerite (TL, nic. //), E : Microphotograph of zoned sphalerite, including galena (TL, nic. //). F: Fe X-ray map of area presented in fig. 10E. The orange rim of sphalerite in fig. 10E corresponds to iron-depleted sphalerite. Note the concentric zoning due to Fe content of smithsonite at the corner right. G to I : transects of Fe and Cd content within sphalerite of figs. 10A, 10D and 10E, illustrating the correlation between both elements. J: sphalerite showing altered orange facies and translucent smithsonite (TL, nic. //). Space between sphalerite crystals is filled by Zn-rich clays (sauconite), carbonate and euhedral crystals of quartz. K: boxwork texture left by dissolved sphalerite, now filled by smithsonite (TL, nic. //). L: sulfides and fragments of quartz cemented by smithsonite (TL, nic. +). M: secondary covellite, galena and greenockite (grn) rimming sphalerite relics within smithsonite (RL, nic. //). N: EDS spectrum and BSE image of secondary sulfide mixture. Abbreviations are given in fig. 7.

Figure 11 The Beni Tajite ore deposit. A: coral fauna within Upper Pliensbachian limestone (TL, nic. +). B: association of galena and calcite crystals in the protore (TL, nic. //). C: botryoidal texture of the cerussite pseudomorph after galena, with relics of galena (RL, nic. //). D: Raman composition map of the cerussite coating galena crystals of fig. 11C. Cerussite, which defines the botryoidal texture (blue), is partly transformed to a second generation of cerussite (red) that forms limited patches. E and F: X-ray diffraction patterns of grey calamine. G: relics of sphalerite replaced by smithsonite, which also includes geodic crystals of quartz (RL, nic. //). H: aggregate of smithsonite and iron oxi-hydroxide encrusted by goethite and psilomelane (coronadite-chalcophanite), themselves rimmed by secondary smithsonite (RL, nic. //). I: section of calcite scalenohedra forming banded calcite that surrounds a vein of massive sulfides (TL, nic. +). Abbreviations are given in fig. 7.

Figure 12 The Aït Labbes (A to E) and Tizi n'Firest (F and G) ore deposits. A: lineaments of nodular pyrite included within sphalerite (RL, nic. //). Pyrite seems to localize the formation of smithsonite after sphalerite. B: massive replacement of nodular pyrite by goethite (dark grey) and hematite (light grey) (RL, nic. //). C: spherulitic zoned smithsonite encrusting aggregates of smithsonite and iron oxi-hydroxide (TL, nic. +). Hemimorphite fills the voids. D: banded and collomorphic smithsonite pigmented by iron oxi-hydroxide (RL, nic. +). E: tabular crystals of hemimorphite containing relics of spherulitic smithsonite, whose zoning is revealed by oxidation (TL, nic. +). F: red calamine (oxidized smithsonite) containing a geode with euhedral crystals of smithsonite at the wall (TL, nic. +). Cavity was further filled by sauconite showing mud cracks. G: X-ray diffraction pattern of clayey material within geodes. Abbreviations are given in fig. 7.

Figure 13 Synoptic paragenetic sequences of observed minerals in each deposit or prospect. Vertical lines represent the separation between the pre-mineralization, the protore mineralization and the supergene stages. Vertical dashed line corresponds to the limit between the red or black calamines and the grey and white calamines.

Figure 14 Geological sketches of the formation processes of the High Atlas non-sulfide Pb-Zn ore deposits. This is an idealized view of the mineralization events; in details, several stages may be reduced or lacking for a given ore deposit. Three stages are proposed: A: emplacement of the ore body within the reefal limestone. B: tilting of strata and uplift result in weathering of ore body by supergene oxidation. C: formation of non-sulfide Zn deposits continues after the total replacement of sulfides above the water table. Direct replacement of the sulfides and filling of the karstic cavities are the major processes, but in this later case, migration of a Zn-bearing solution remains limited. No wall rock replacement has been observed. This evolution is very similar to that proposed by Reichert and Borg (2009) for the Zn non-sulfide ore deposits in Iran.

Figure 15 Tectonic sketches illustrating the development of the non-sulfide Pb-Zn deposit during the evolution of the Moroccan High Atlas. The opening of Atlantic Ocean and Tethys (A) is accommodated by normal faults. The role of these faults to serve as conduits for mineralizing fluids has been suggested by Mouguina (2004), but the hypothesis of intrabasinal flows can not be ruled out. During Cenozoic (B), these faults were reactivated as thrusts that accommodate the formation of anticline, related to the High Atlas intra-continental belt. Folding has caused a verticalization of the stratiform lenses of sulfides and has been followed by successive uplift periods, until Present, which have facilitated the percolation of meteoritic water, the karst formation and the subsequent replacement of sulfides by calamine (C).

Table 1: Average WDS analyses (%wt) and average value of cations per formula unit for sulfides and carbonates from Toulal (T4a, TH3), Tadaghast (TA4, TA10) and Beni Tajite (BT17). Structural formulae of sulfides were carried out assuming a total sum of atoms of 2. Structural formulae of carbonates are based on a total sum of cations of 2. The corresponding average of calculated CO2 content and sum are also provided. Avg.: average, SD: standard deviation, RSD: relative standard deviation (RSD=(SD/Avg.)x100), n: number of analyses, n.d.: non-detected. For other abbreviations, see figure 7. For sulfides, only data with total in the range of 97-103% were used for average calculation (avg.). Each individual data was considered significant at 95 and 99% of confidence level if: $N_S \cdot t_s - N_B \cdot t_B > k\sqrt{N_B \cdot t_B}$ where is the count number by second of sample peak, is the counting time of sample peak, is the count number by second of background, is the counting time of background and k is equal to either 2 for a risk of 5%, or 3 for a risk of 1%.

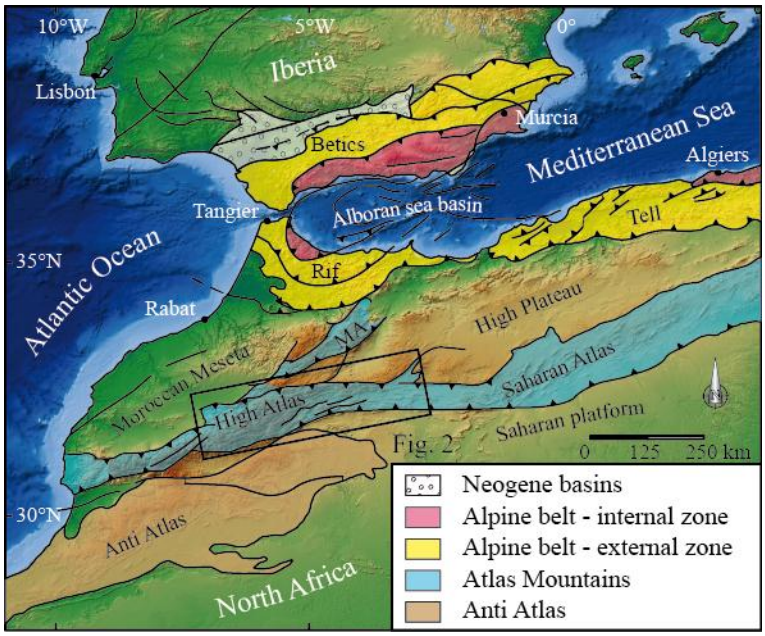
10°W
5°W
0°
Iberia
Lisbon
Murcia
Mediterranean Sea
Betics
Algiers
Tangier
Alboran sea basin
Tell
35°N
Atlantic Ocean
Rif
Rabat
High Plateau
MA
Moroccan Meseta
Saharan Atlas
High Atlas
Fig. 2
Saharan platform
0 125 250 km
30°N
Anti Atlas
North Africa
Neogene basins
Alpine belt - internal zone
Alpine belt - external zone
Atlas Mountains
Anti Atlas

Figure 1

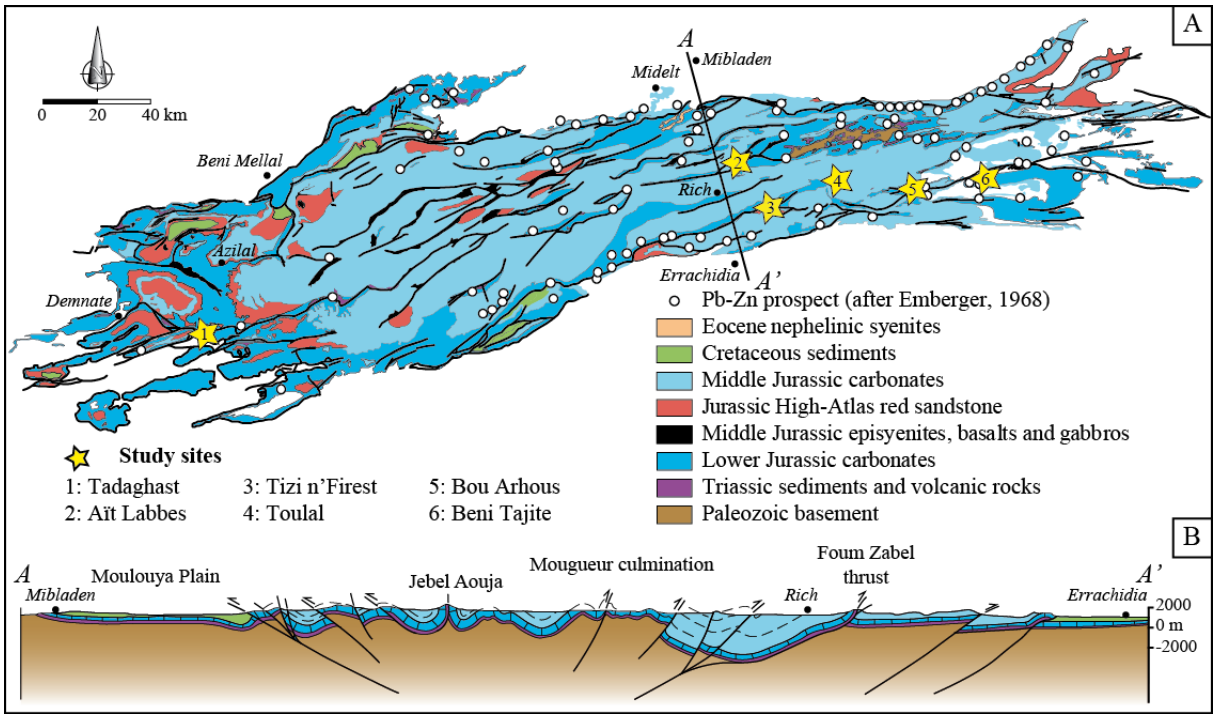
A
N
0 20 40 km
A
Midelt
Mibladen
Beni Mellal
Rich
Azilal
Errachidia
A'
Demnate
Pb-Zn prospect (after Emberger, 1968)
Eocene nephelinic syenites
Cretaceous sediments
Middle Jurassic carbonates
Jurassic High-Atlas red sandstone
Middle Jurassic episyenites, basalts and gabbros
Lower Jurassic carbonates
Triassic sediments and volcanic rocks
Paleozoic basement
Study sites
1: Tadaghast
2: Aït Labbes
3: Tizi n'Firest
4: Toulal
5: Bou Arhous
6: Beni Tajite
B
A
Mibladen
Moulouya Plain
Jebel Aouja
Mougueur culmination
Foum Zabel thrust
Rich
A'
Errachidia
2000
0 m
-2000

Figure 2

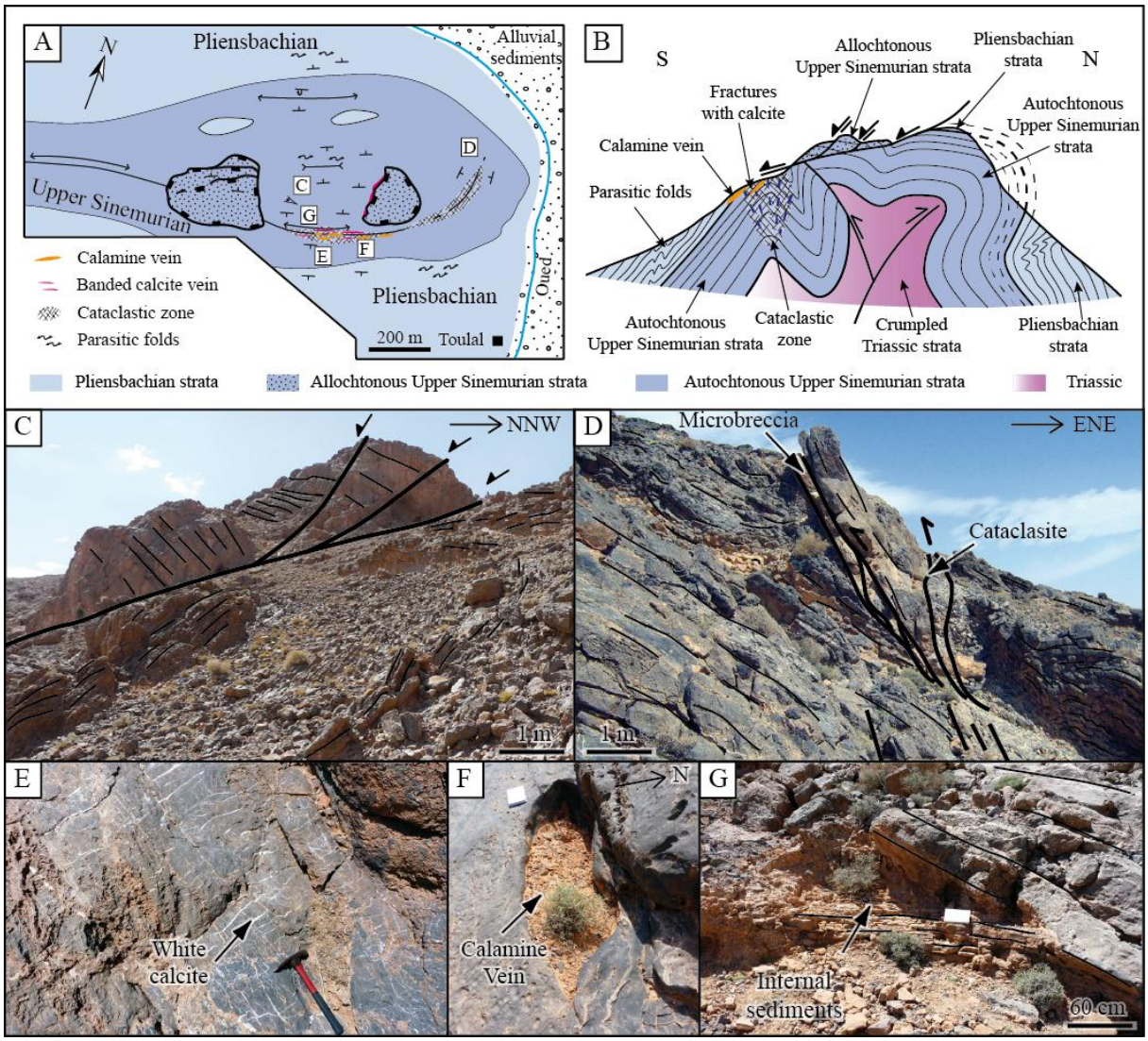
A
N
Pliensbachian
Alluvial sediments
Upper Sinemurian
Pliensbachian
Oued
200 m
Toulal
Calamine vein
Banded calcite vein
Cataclastic zone
Parasitic folds
B
S
N
Allochtonous Upper Sinemurian strata
Pliensbachian strata
Fractures with calcite
Calamine vein
Parasitic folds
Autochtonous Upper Sinemurian strata
Autochtonous Upper Sinemurian strata
Cataclastic zone
Crumpled Triassic strata
Pliensbachian strata
Pliensbachian strata
Allochtonous Upper Sinemurian strata
Autochtonous Upper Sinemurian strata
Triassic
C
NNW
1 m
D
Microbreccia
ENE
Cataclasite
1 m
E
White calcite
F
N
Calamine Vein
G
Infernal sediments
60 cm

Figure 3

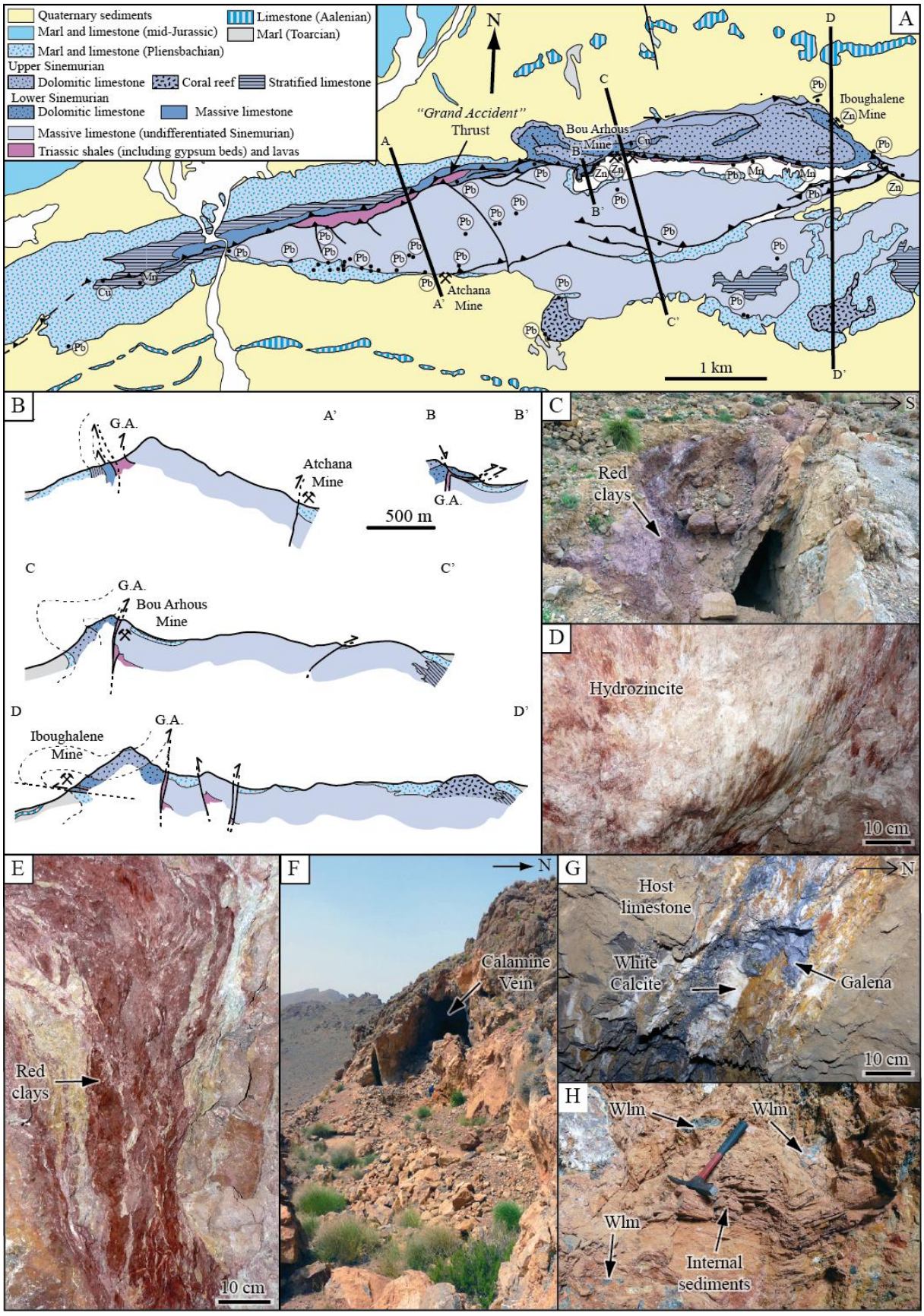
Quaternary sediments
Marl and limestone (mid-Jurassic)
Marl and limestone (Pliensbachian)
Upper Sinemurian
Dolomitic limestone
Coral reef
Stratified limestone
Lower Sinemurian
Dolomitic limestone
Massive limestone
Massive limestone (undifferentiated Sinemurian)
Triassic shales (including gypsum beds) and lavas
Limestone (Aalenian)
Marl (Toarcian)
A
N
"Grand Accident" Thrust
Bou Arhous Mine
Iboughalene Mine
Atchana Mine
1 km
B
G.A.
500 m
C
S
Red clays
D
Hydrozincite
10 cm
E
Red clays
10 cm
F
N
Calamine Vein
G
N
Host limestone
White Calcite
Galena
10 cm
H
Wlm
Internal sediments

Figure 4

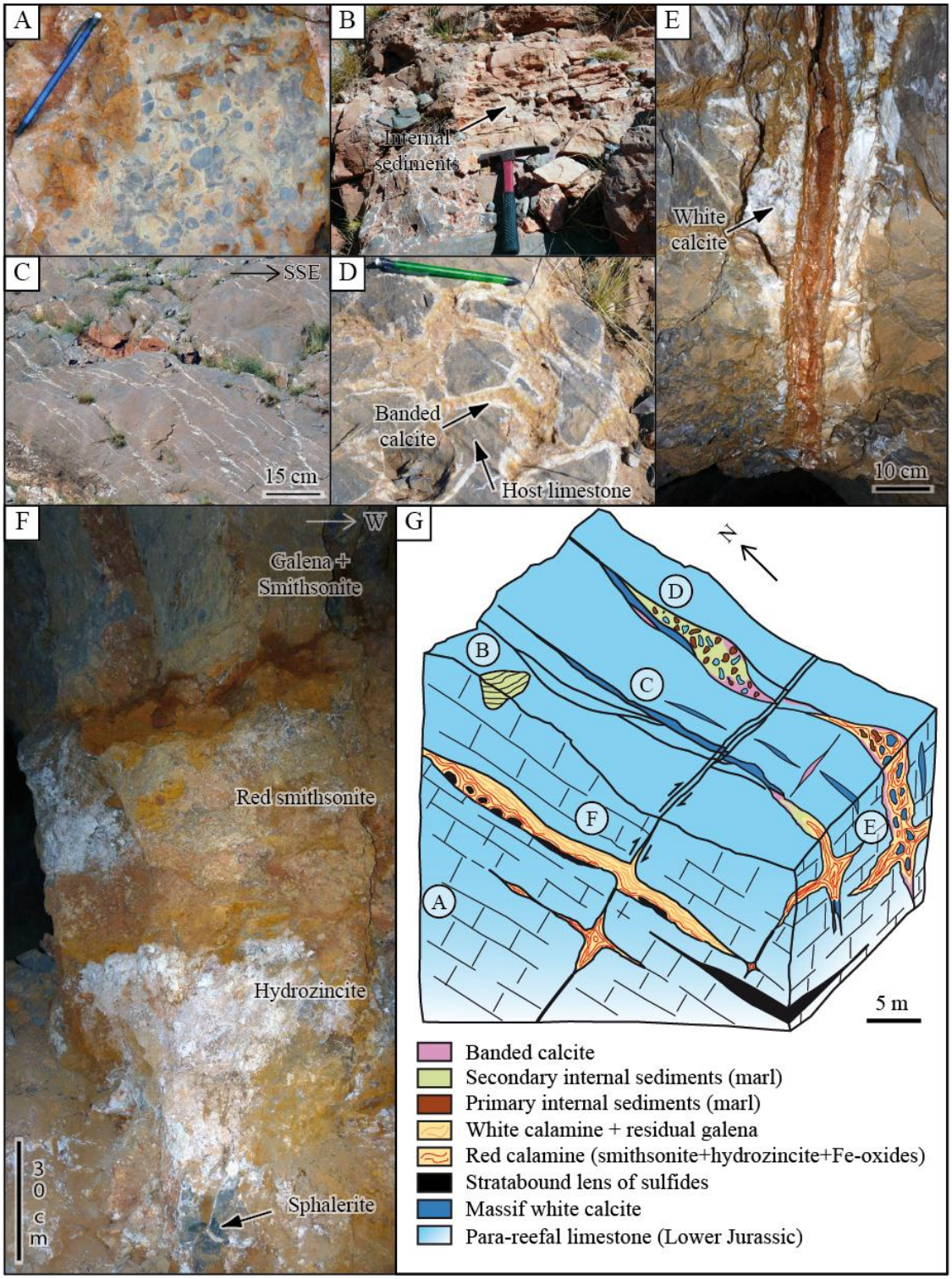
A
B
Internal sediments
E
White calcite
C
SSE
15 cm
D
Banded calcite
Host limestone
10 cm
F
W
Galena + Smithsonite
Red smithsonite
Hydrozincite
30 cm
Sphalerite
G
N
D
B
C
F
E
A
5 m
Banded calcite
Secondary internal sediments (marl)
Primary internal sediments (marl)
White calamine + residual galena
Red calamine (smithsonite+hydrozincite+Fe-oxides)
Stratabound lens of sulfides
Massif white calcite
Para-reefal limestone (Lower Jurassic)

Figure 5

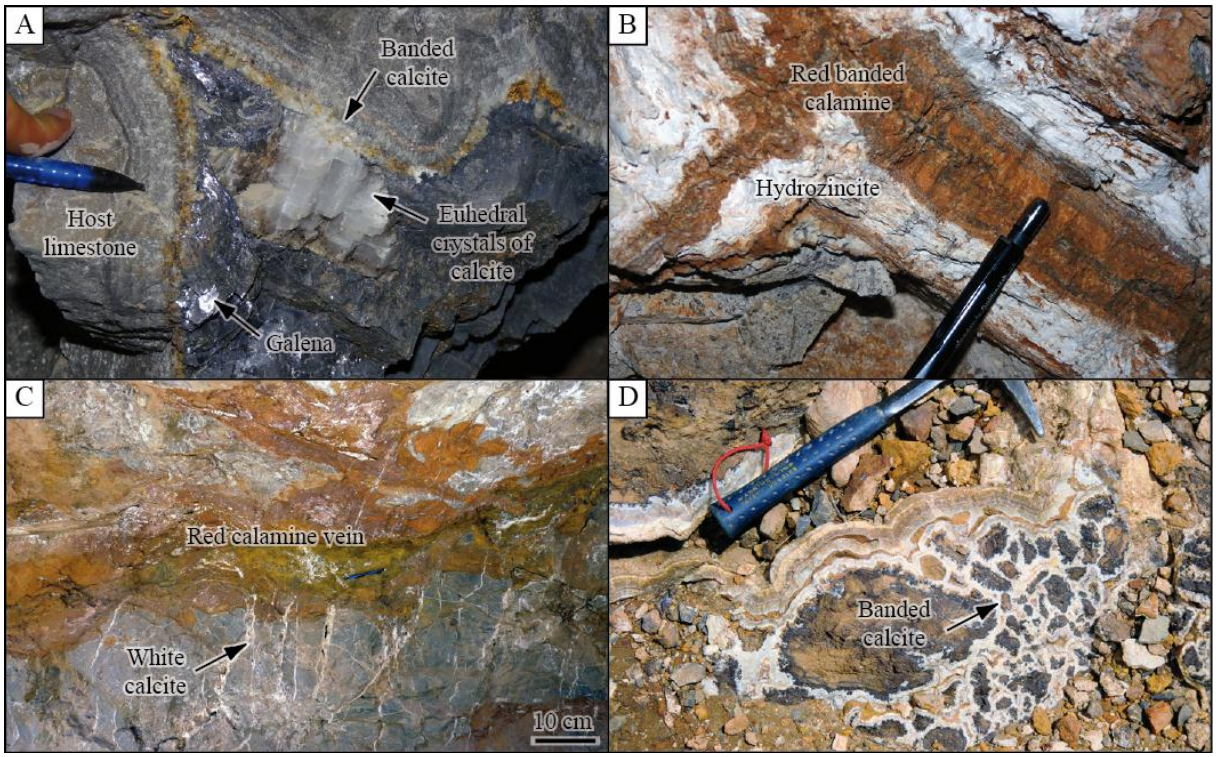
A
Banded calcite
Host limestone
Euhedral crystals of calcite
Galena
B
Red banded calamine
Hydrozincite
C
Red calamine vein
White calcite
10 cm
D
Banded calcite

Figure 6

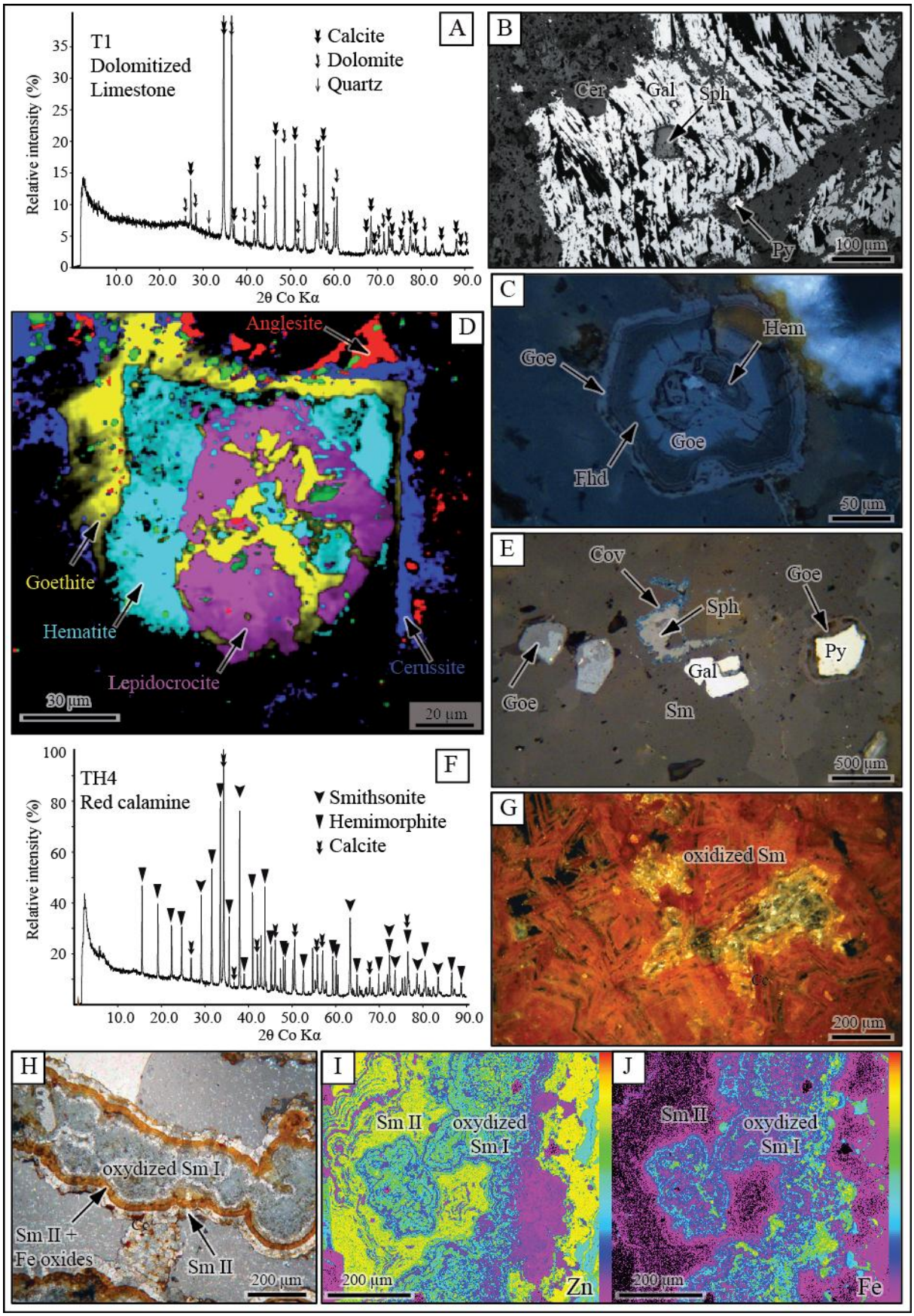
A
T1
Dolomitized
Limestone
Calcite
Dolomite
Quartz
Relative intensity (%)
2θ Co Kα
B
Cer
Gal
Sph
Py
100 µm
C
Hem
Goe
Goe
Fhd
50 µm
D
Anglesite
Goethite
Hematite
Lepidocrocite
Cerussite
30 µm
20 µm
E
Cov
Goe
Sph
Py
Gal
Goe
Sm
500 µm
F
TH4
Red calamine
Smithsonite
Hemimorphite
Calcite
Relative intensity (%)
2θ Co Kα
G
oxidized Sm
Cc
200 µm
H
oxydized Sm I
Sm II +
Fe oxides
Cc
Sm II
200 µm
I
Sm II
oxydized
Sm I
200 µm
Zn
J
Sm II
oxydized
Sm I
200 µm
Fe

Figure 7

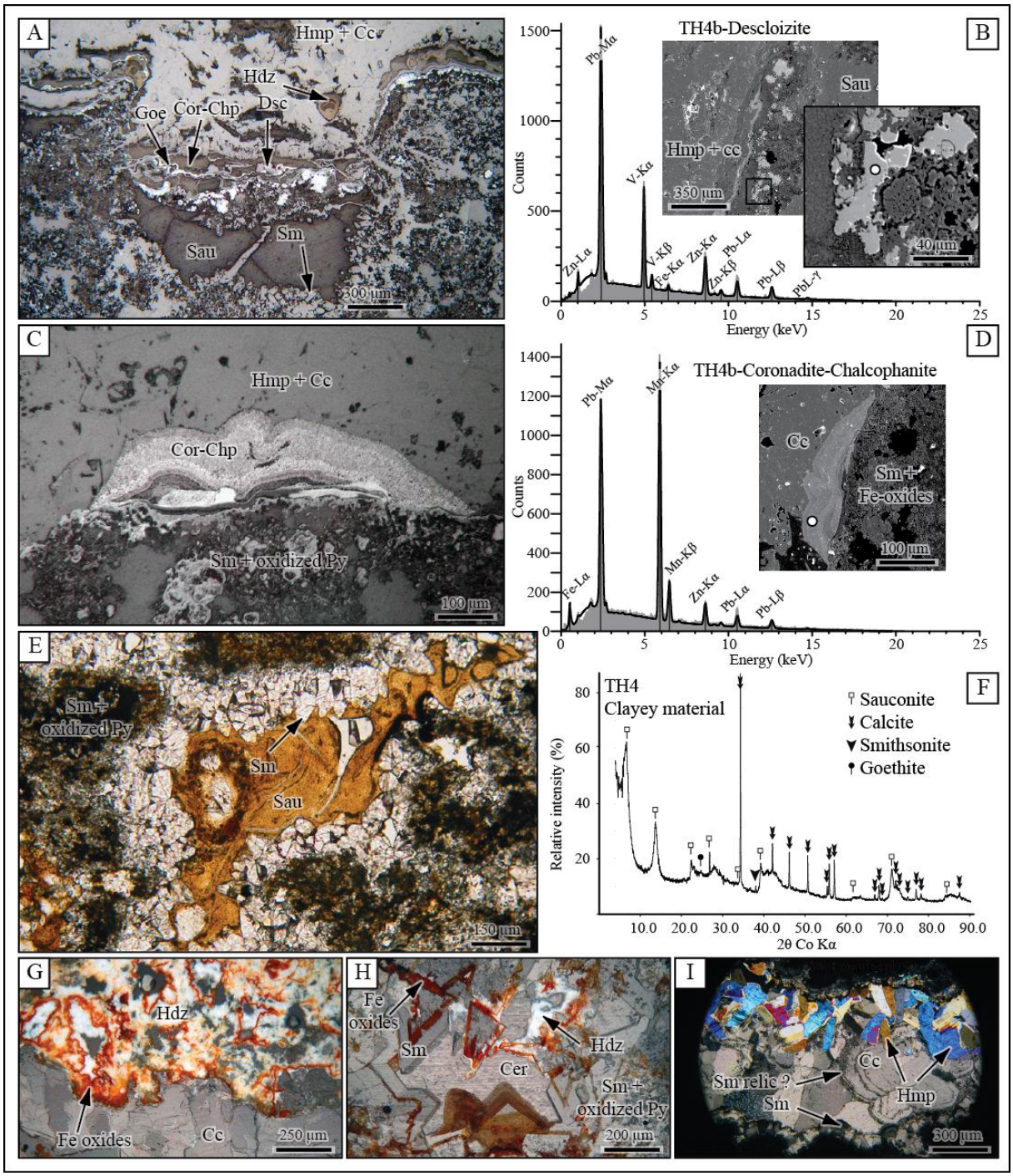
A
Hmp + Cc
Hdz
Goe
Cor-Chp
Dsc
Sau
Sm
300 µm
B
TH4b-Descloizite
Pb-Mα
V-Kα
Zn-Lα
V-Kβ
Fe-Kα
Zn-Kα
Pb-Lα
Zn-Kβ
Pb-Lβ
PbL-γ
Counts
Energy (keV)
Sau
Hmp + cc
350 µm
40 µm
C
Hmp + Cc
Cor-Chp
Sm + oxidized Py
100 µm
D
TH4b-Coronadite-Chalcophanite
Pb-Mα
Mn-Kα
Fe-Lα
Mn-Kβ
Zn-Kα
Pb-Lα
Pb-Lβ
Counts
Energy (keV)
Cc
Sm + Fe-oxides
100 µm
E
Sm + oxidized Py
Sm
Sau
150 µm
F
TH4
Clayey material
Sauconite
Calcite
Smithsonite
Goethite
Relative intensity (%)
2θ Co Kα
G
Hdz
Fe oxides
Cc
250 µm
H
Fe oxides
Sm
Cer
Hdz
Sm + oxidized Py
200 µm
I
Sm relic ?
Sm
Cc
Hmp
300 µm

Figure 8

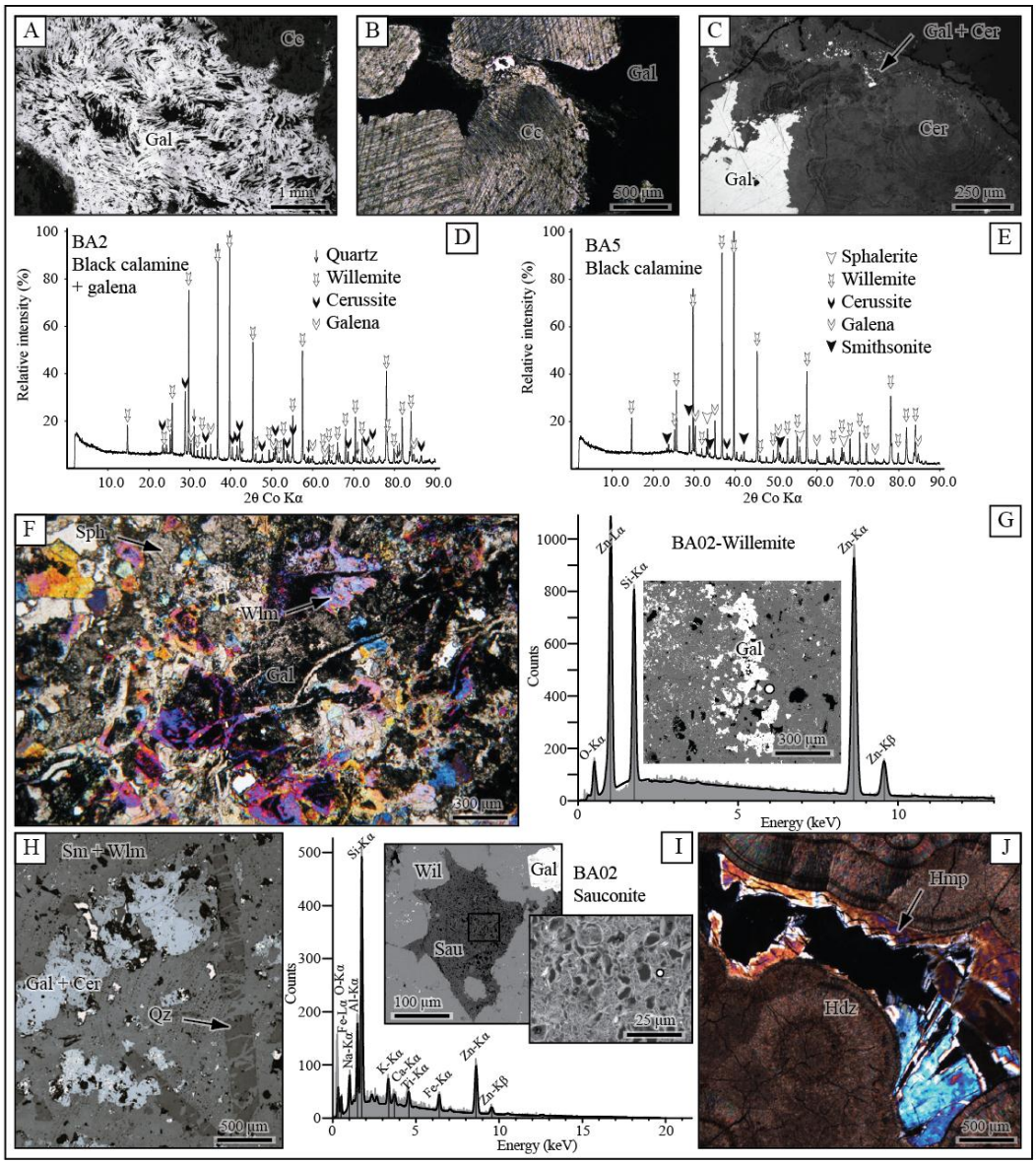
A
Cc
Gal
1 mm
B
Gal
Cc
500 µm
C
Gal + Cer
Cer
Gal
250 µm
D
BA2
Black calamine
+ galena
Quartz
Willemite
Cerussite
Galena
Relative intensity (%)
2θ Co Kα
E
BA5
Black calamine
Sphalerite
Willemite
Cerussite
Galena
Smithsonite
Relative intensity (%)
2θ Co Kα
F
Sph
Wlm
Gal
300 µm
G
BA02-Willemite
Zn-Lα
Si-Kα
Zn-Kα
O-Kα
Zn-Kβ
Gal
300 µm
Counts
Energy (keV)
H
Sm + Wlm
Gal + Cer
Qz
500 µm
I
BA02
Sauconite
Wil
Gal
Sau
100 µm
25 µm
Si-Kα
Fe-Lα
O-Kα
Al-Kα
Na-Kα
K-Kα
Ca-Kα
Ti-Kα
Fe-Kα
Zn-Kα
Zn-Kβ
Counts
Energy (keV)
J
Hmp
Hdz
500 µm

Figure 9

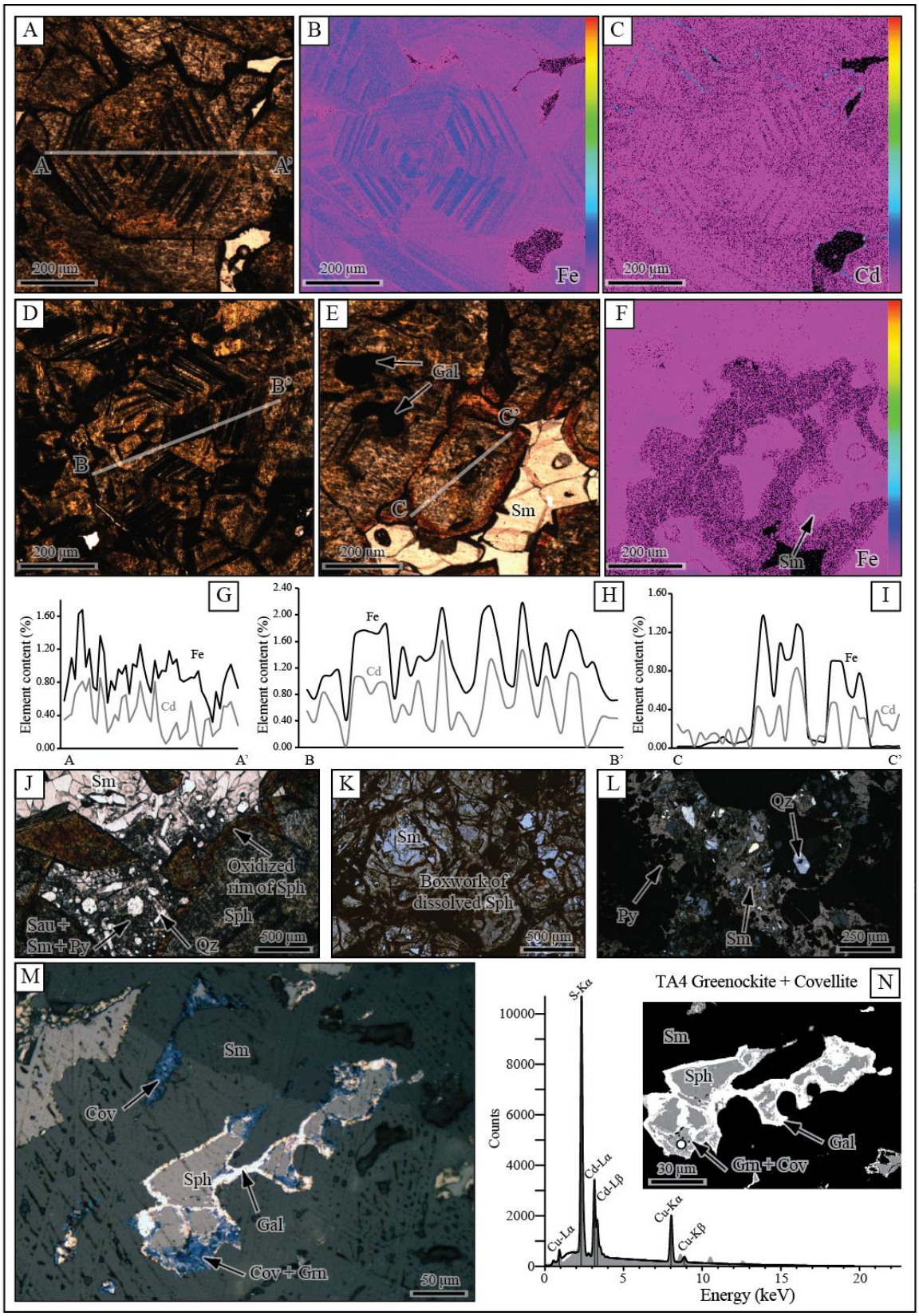
A
A'
200 µm
B
Fe
C
Cd
D
B'
B
E
Gal
C'
C
Sm
F
G
Element content (%)
Fe
Cd
H
I
J
Sm
Oxidized rim of Sph
Sph
Sau + Sm + Py
Qz
500 µm
K
Boxwork of dissolved Sph
L
Py
250 µm
M
Cov
Cov + Grn
50 µm
TA4 Greenockite + Covellite
N
Counts
Energy (keV)
S-Kα
Cd-Lα
Cd-Lβ
Cu-Kα
Cu-Kβ
Cu-Lα
Grn + Cov
30 µm

Figure 10

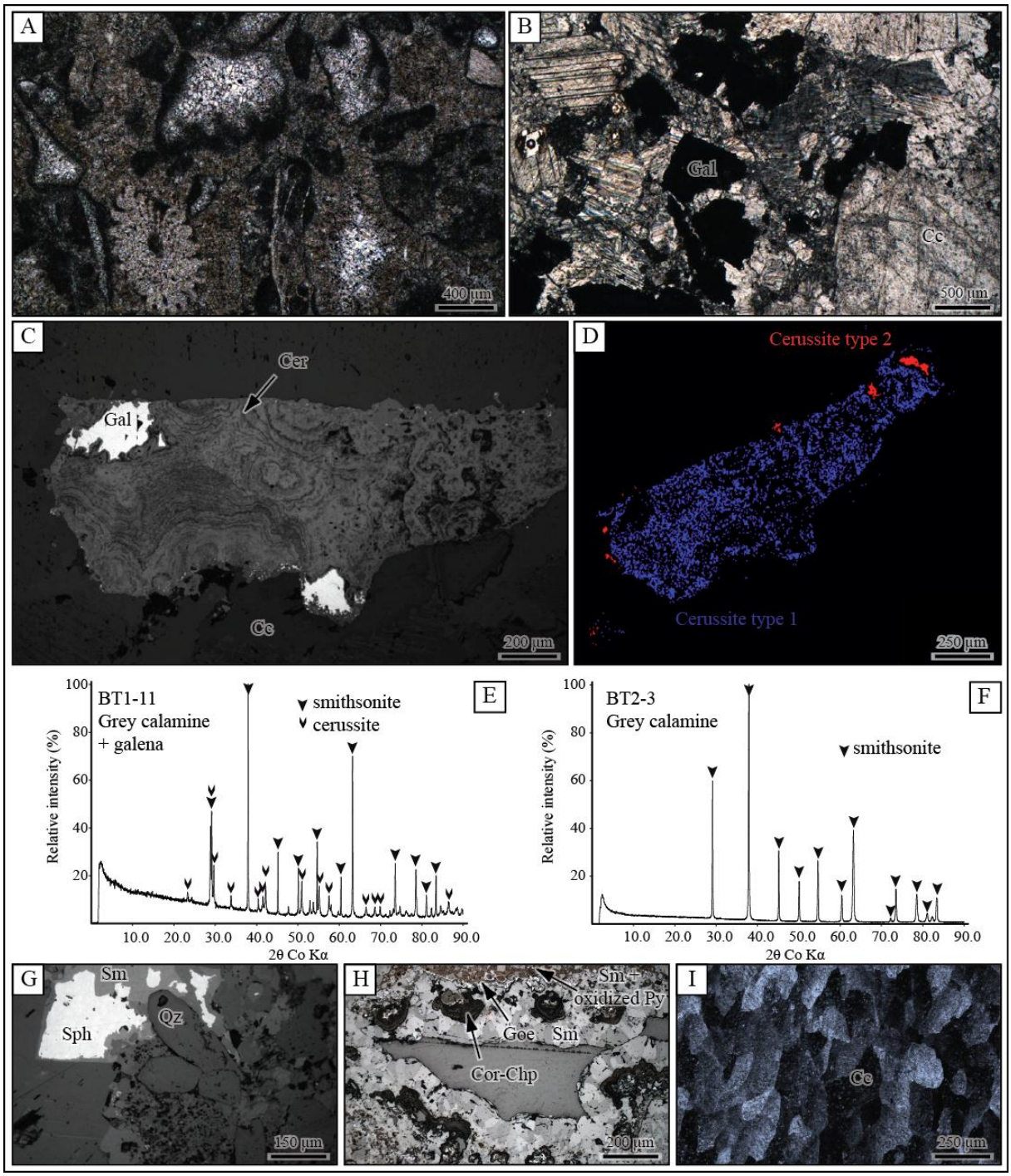
A
400 µm
B
Gal
Cc
500 µm
C
Cer
Gal
Cc
200 µm
D
Cerussite type 2
Cerussite type 1
250 µm
E
BT1-11
Grey calamine
+ galena
smithsonite
cerussite
Relative intensity (%)
2θ Co Kα
F
BT2-3
Grey calamine
smithsonite
Relative intensity (%)
2θ Co Kα
G
Sm
Qz
Sph
150 µm
H
Sm + oxidized Py
Goe
Sm
Cor-Chp
200 µm
I
Cc
250 µm

Figure 11

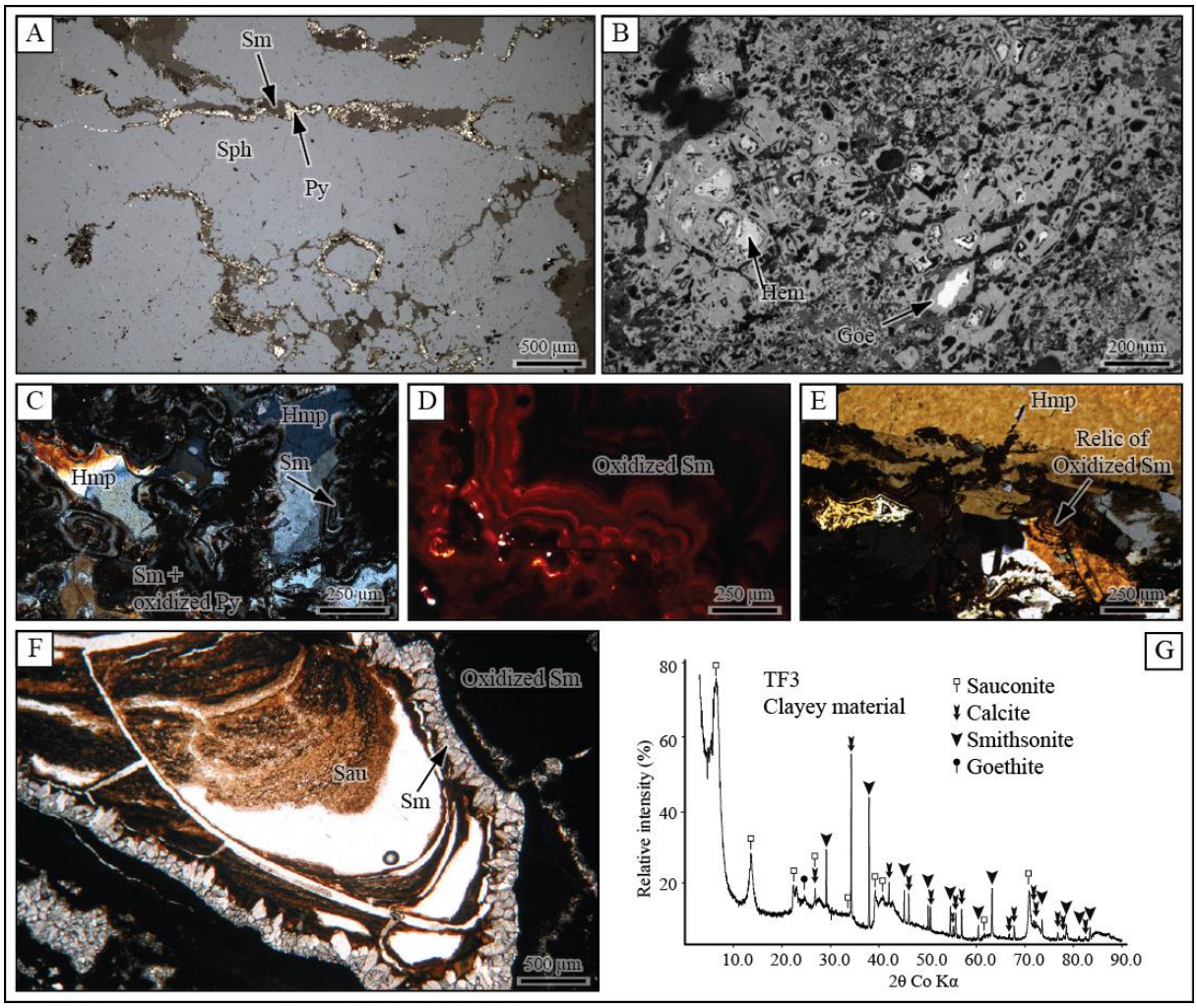
A
Sm
Sph
Py
500 µm
B
Hem
Goe
200 µm
C
Hmp
Hmp
Sm
Sm +
oxidized Py
250 µm
D
Oxidized Sm
250 µm
E
Hmp
Relic of
Oxidized Sm
250 µm
F
Oxidized Sm
Sau
Sm
500 µm
G
TF3
Clayey material
Sauconite
Calcite
Smithsonite
Goethite
Relative intensity (%)
80
60
40
20
10.0
20.0
30.0
40.0
50.0
60.0
70.0
80.0
90.0
2θ Co Kα

Figure 12

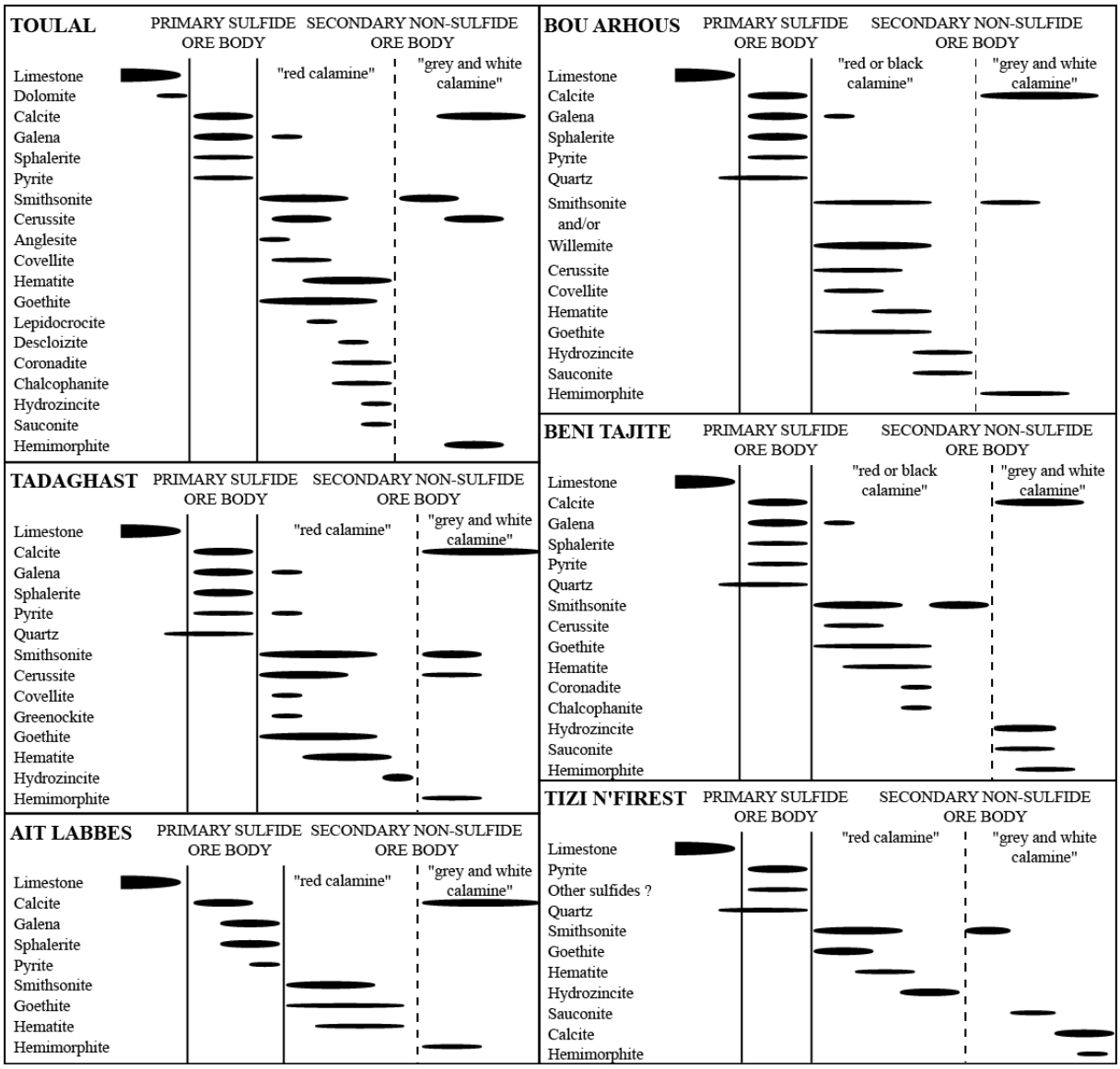
TOULAL
PRIMARY SULFIDE ORE BODY
SECONDARY NON-SULFIDE ORE BODY
"red calamine"
"grey and white calamine"
Limestone
Dolomite
Calcite
Galena
Sphalerite
Pyrite
Smithsonite
Cerussite
Anglesite
Covellite
Hematite
Goethite
Lepidocrocite
Descloizite
Coronadite
Chalcophanite
Hydrozincite
Sauconite
Hemimorphite
TADAGHAST
PRIMARY SULFIDE ORE BODY
SECONDARY NON-SULFIDE ORE BODY
"red calamine"
"grey and white calamine"
Limestone
Calcite
Galena
Sphalerite
Pyrite
Quartz
Smithsonite
Cerussite
Covellite
Greenockite
Goethite
Hematite
Hydrozincite
Hemimorphite
AIT LABBES
PRIMARY SULFIDE ORE BODY
SECONDARY NON-SULFIDE ORE BODY
"red calamine"
"grey and white calamine"
Limestone
Calcite
Galena
Sphalerite
Pyrite
Smithsonite
Goethite
Hematite
Hemimorphite
BOU ARHOUS
PRIMARY SULFIDE ORE BODY
SECONDARY NON-SULFIDE ORE BODY
"red or black calamine"
"grey and white calamine"
Limestone
Calcite
Galena
Sphalerite
Pyrite
Quartz
Smithsonite and/or
Willemite
Cerussite
Covellite
Hematite
Goethite
Hydrozincite
Sauconite
Hemimorphite
BENI TAJITE
PRIMARY SULFIDE ORE BODY
SECONDARY NON-SULFIDE ORE BODY
"red or black calamine"
"grey and white calamine"
Limestone
Calcite
Galena
Sphalerite
Pyrite
Quartz
Smithsonite
Cerussite
Goethite
Hematite
Coronadite
Chalcophanite
Hydrozincite
Sauconite
Hemimorphite
TIZI N'FIREST
PRIMARY SULFIDE ORE BODY
SECONDARY NON-SULFIDE ORE BODY
"red calamine"
"grey and white calamine"
Limestone
Pyrite
Other sulfides ?
Quartz
Smithsonite
Goethite
Hematite
Hydrozincite
Sauconite
Calcite
Hemimorphite

Figure 13

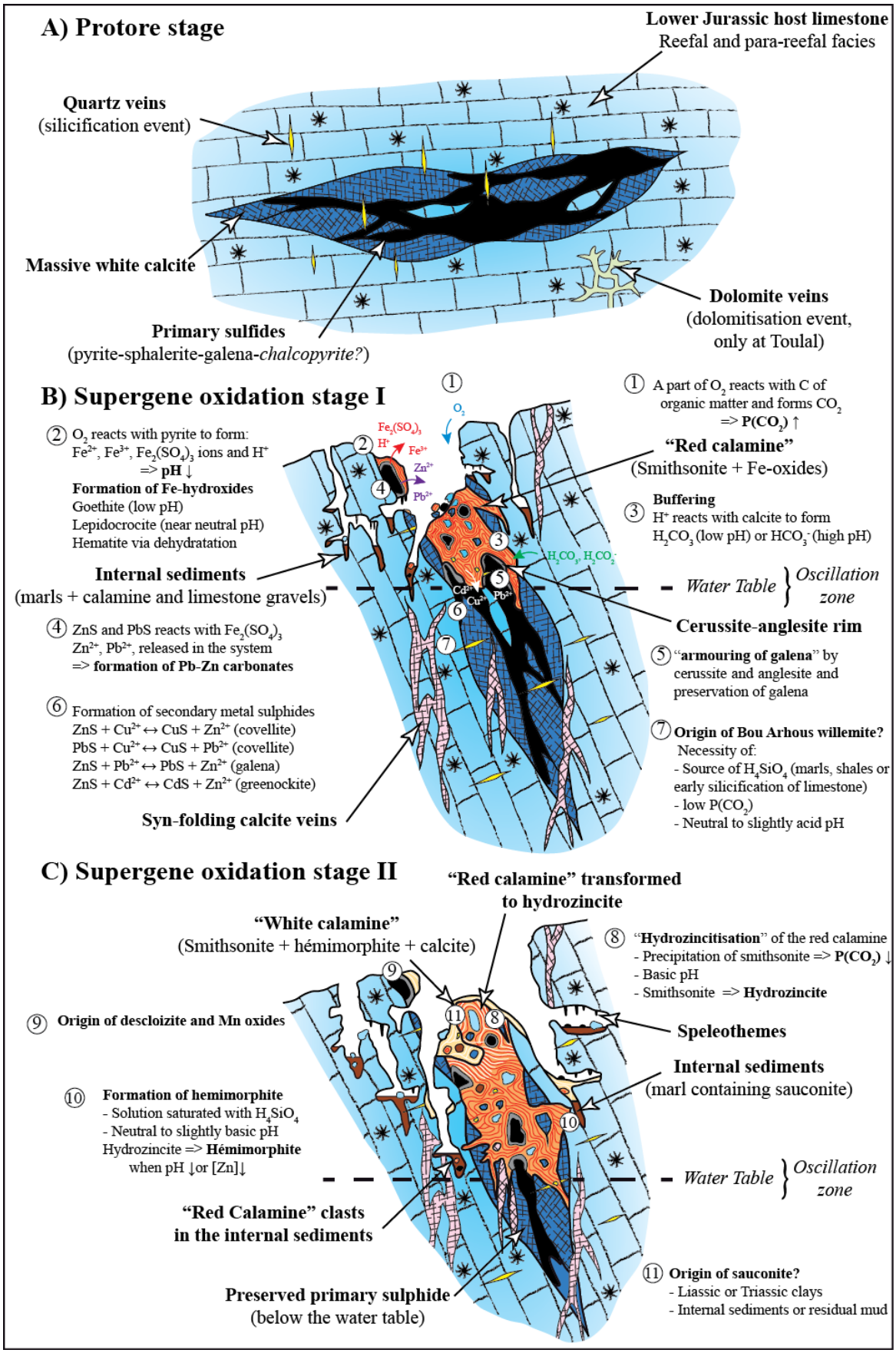
A) Protore stage
Lower Jurassic host limestone
Reefal and para-reefal facies
Quartz veins
(silicification event)
Massive white calcite
Primary sulfides
(pyrite-sphalerite-galena-chalcopyrite?)
Dolomite veins
(dolomitisation event, only at Toulal)
B) Supergene oxidation stage I
① A part of O2 reacts with C of organic matter and forms CO2 => P(CO2) ↑
② O2 reacts with pyrite to form: Fe2+, Fe3+, Fe2(SO4)3 ions and H+ => pH ↓
Formation of Fe-hydroxides
Goethite (low pH)
Lepidocrocite (near neutral pH)
Hematite via dehydratation
"Red calamine"
(Smithsonite + Fe-oxides)
③ Buffering
H+ reacts with calcite to form H2CO3 (low pH) or HCO3- (high pH)
Internal sediments
(marls + calamine and limestone gravels)
Water Table
Oscillation zone
Cerussite-anglesite rim
④ ZnS and PbS reacts with Fe2(SO4)3
Zn2+, Pb2+, released in the system
=> formation of Pb-Zn carbonates
⑤ "armouring of galena" by cerussite and anglesite and preservation of galena
⑥ Formation of secondary metal sulphides
ZnS + Cu2+ ↔ CuS + Zn2+ (covellite)
PbS + Cu2+ ↔ CuS + Pb2+ (covellite)
ZnS + Pb2+ ↔ PbS + Zn2+ (galena)
ZnS + Cd2+ ↔ CdS + Zn2+ (greenockite)
⑦ Origin of Bou Arhous willemite?
Necessity of:
- Source of H4SiO4 (marls, shales or early silicification of limestone)
- low P(CO2)
- Neutral to slightly acid pH
Syn-folding calcite veins
C) Supergene oxidation stage II
"Red calamine" transformed to hydrozincite
"White calamine"
(Smithsonite + hémimorphite + calcite)
⑧ "Hydrozincitisation" of the red calamine
- Precipitation of smithsonite => P(CO2) ↓
- Basic pH
- Smithsonite => Hydrozincite
⑨ Origin of descloizite and Mn oxides
Speleothemes
Internal sediments
(marl containing sauconite)
⑩ Formation of hemimorphite
- Solution saturated with H4SiO4
- Neutral to slightly basic pH
Hydrozincite => Hémimorphite when pH ↓or [Zn]↓
Water Table
Oscillation zone
"Red Calamine" clasts in the internal sediments
Preserved primary sulphide
(below the water table)
⑪ Origin of sauconite?
- Liassic or Triassic clays
- Internal sediments or residual mud

Figure 14

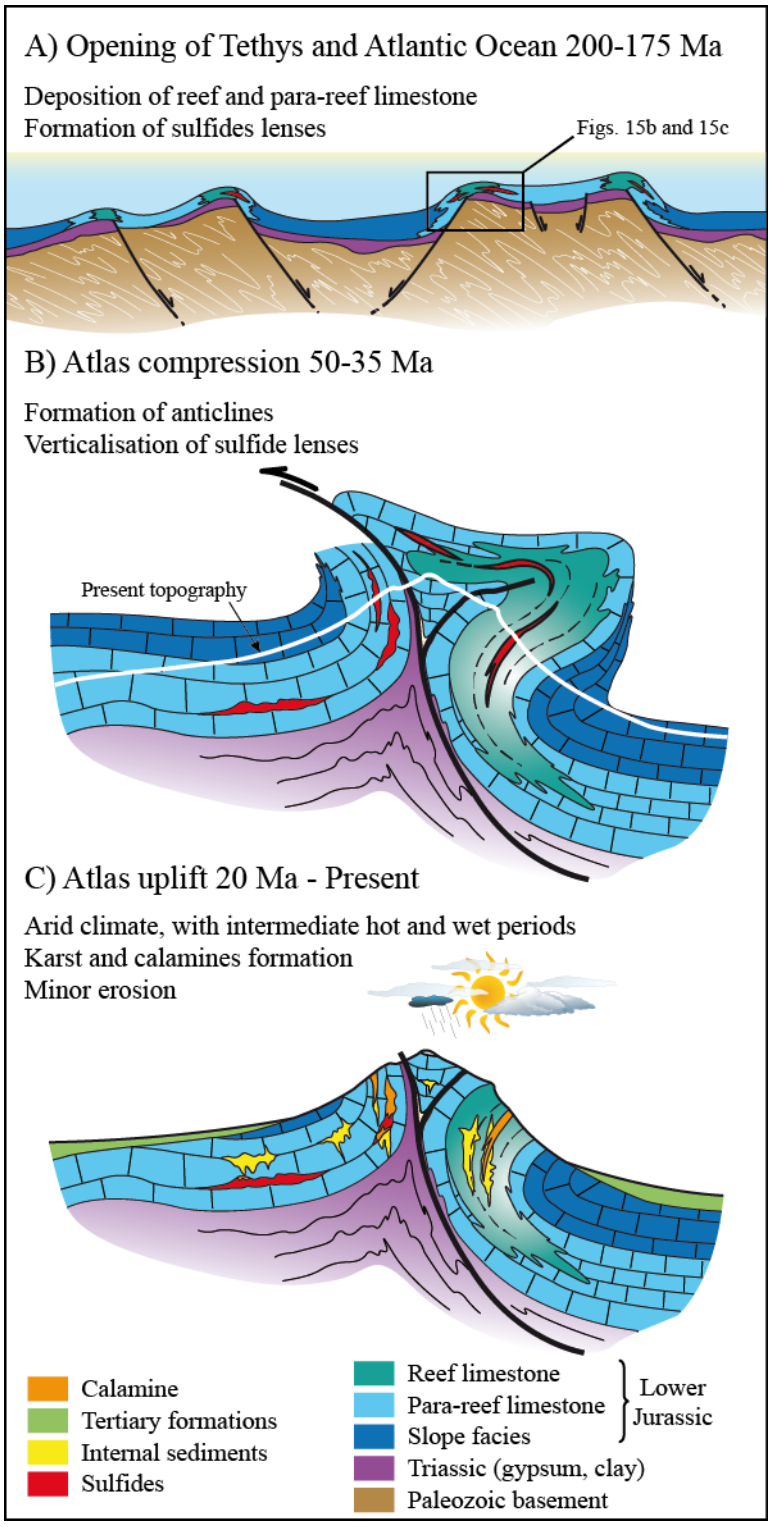
A) Opening of Tethys and Atlantic Ocean 200-175 Ma
Deposition of reef and para-reef limestone
Formation of sulfides lenses
Figs. 15b and 15c
B) Atlas compression 50-35 Ma
Formation of anticlines
Verticalisation of sulfide lenses
Present topography
C) Atlas uplift 20 Ma - Present
Arid climate, with intermediate hot and wet periods
Karst and calamines formation
Minor erosion
Calamine
Tertiary formations
Internal sediments
Sulfides
Reef limestone
Para-reef limestone
Slope facies
Lower Jurassic
Triassic (gypsum, clay)
Paleozoic basement

Figure 15

Table 1

| | T4a | | | | | | | | | TA4 | | | | | | TA10 | | | | | |
|---|---|---|---|---|---|---|---|---|---|---|---|---|---|---|---|---|---|---|---|---|---|
| | Sph (n=8) | | | Gal I (n=9) | | | Gal II (n=6) | | | Sph (n=16) | | | Sph (n=128) | | | Gal (n=11) | | | | |
| | Avg. (%) | SD | RSD (%) | Avg. (%) | SD | RSD (%) | Avg. (%) | SD | RSD (%) | Avg. (%) | SD | RSD (%) | Avg. (%) | SD | RSD (%) | Avg. (%) | SD | RSD (%) | | |
| Pb | 0,05 | 0,06 | 114,24 | 87,23 | 0,34 | 0 | 83,12 | 4,14 | 5 | 0,07 | 0,08 | 115 | 0,07 | 0,09 | 128 | 86,71 | 0,61 | 1 | | |
| Sb | 0,02 | 0,02 | 157,12 | 0,01 | 0,02 | 187 | n.d. | | | 0,01 | 0,01 | 206 | n.d. | | | n.d. | | | | |
| Zn | 66,34 | 0,43 | 0,64 | n.d. | | | 5,79 | 1,13 | 20 | 65,73 | 1,39 | 2 | 65,26 | 1,05 | 2 | 0,45 | 0,65 | 144 | | |
| Fe | 1,20 | 0,27 | 22,20 | n.d. | | | 0,20 | 0,22 | 114 | 0,99 | 0,18 | 19 | 0,86 | 0,53 | 62 | n.d. | | | | |
| S | 32,44 | 0,21 | 0,65 | 13,12 | 0,10 | 1 | 11,37 | 2,61 | 23 | 32,55 | 0,26 | 1 | 32,02 | 0,33 | 1 | 12,74 | 0,10 | 1 | | |
| Cu | 0,01 | 0,01 | 106,98 | n.d. | | | 0,18 | 0,41 | 224 | 0,32 | 0,54 | 169 | 0,08 | 0,10 | 127 | n.d. | | | | |
| Ag | 0,01 | 0,01 | 185,59 | 0,01 | 0,02 | 157 | 0,01 | 0,02 | 145 | n.d. | | | 0,01 | 0,03 | 216 | 0,01 | 0,02 | 261 | | |
| Ni | n.d. | | | n.d. | | | 0,00 | | | n.d. | | | n.d. | | | n.d. | | | | |
| Bi | 0,09 | 0,08 | 85,45 | 0,76 | 0,23 | 31 | 0,60 | 0,05 | 8 | 0,13 | 0,10 | 82 | 0,07 | 0,08 | 118 | 0,76 | 0,12 | 16 | | |
| As | n.d. | | | n.d. | | | n.d. | | | 0,01 | 0,03 | 387 | n.d. | | | n.d. | | | | |
| Co | n.d. | | | n.d. | | | n.d. | | | n.d. | | | n.d. | | | n.d. | | | | |
| Cd | 0,21 | 0,04 | 18,66 | n.d. | | | 0,49 | 1,05 | 212 | 0,40 | 0,56 | 142 | 0,42 | 0,33 | 78 | n.d. | | | | |
| Ge | n.d. | | | n.d. | | | n.d. | | | n.d. | | | 0,00 | 0,01 | 816 | n.d. | | | | |
| Total | 100,35 | 0,39 | 0,38 | 101,14 | 0,45 | 0 | 101,77 | 5,73 | 6 | 100,20 | 0,69 | 1 | 98,79 | 0,75 | 1 | 100,68 | 0,78 | 1 | | |
| | Average cations per formula unit | | | | | | | | | | | | | | | | | | | |
| Pb | | | | 0,99 | | | 0,80 | | | | | | | | | 0,98 | | | | |
| Sb | | | | | | | | | | | | | | | | | | | | |
| Zn | 0,98 | | | | | | 0,18 | | | 0,97 | | | 0,98 | | | 0,02 | | | | |
| Fe | 0,02 | | | | | | 0,01 | | | 0,02 | | | 0,02 | | | | | | | |
| S | 0,97 | | | 0,96 | | | 0,70 | | | 0,98 | | | 0,98 | | | 0,93 | | | | |
| Cu | | | | | | | 0,01 | | | | | | | | | | | | | |
| Ag | | | | | | | | | | | | | | | | | | | | |
| Ni | | | | | | | | | | | | | | | | 0,00 | | | | |
| Bi | | | | 0,01 | | | 0,01 | | | | | | | | | 0,01 | | | | |
| As | | | | | | | | | | | | | | | | 0,00 | | | | |
| Co | | | | | | | | | | | | | | | | 0,00 | | | | |
| Cd | | | | | | | 0,01 | | | | | | | | | 0,00 | | | | |
| Ge | | | | | | | | | | | | | | | | 0,00 | | | | |
| Sum | 1,97 | | | 1,96 | | | 1,70 | | | 1,98 | | | 1,98 | | | 1,93 | | | | |

| | TH3a | | | | | | TA4 | | | | | | BT17 | | | | | |
|---|---|---|---|---|---|---|---|---|---|---|---|---|---|---|---|---|---|---|
| | Sm I (n=13) | | | Sm II, n=16 | | | Sm (n=17) | | | Oxydized (n=4) | | | Sm (n=23) | | | Cer (n=11) | | |
| | Avg. (%) | SD | RSD (%) | Avg. (%) | SD | RSD (%) | Avg. (%) | SD | RSD (%) | Avg. (%) | SD | RSD (%) | Avg. (%) | SD | RSD (%) | Avg. (%) | SD | RSD (%) |
| CaO | 0,32 | 0,10 | 31,51 | 0,28 | 0,20 | 72 | 0,13 | 0,16 | 122 | 0,05 | 0,03 | 67 | 0,85 | 0,59 | 69 | 0,03 | 0,04 | 120 |
| SrO | 0,01 | 0,02 | 195,20 | 0,01 | 0,02 | 217 | 0,02 | 0,03 | 124 | 0,04 | 0,04 | 100 | 0,02 | 0,03 | 194 | 0,11 | 0,11 | 101 |
| MgO | 0,63 | 0,39 | 62,78 | 0,53 | 0,88 | 166 | 0,18 | 0,20 | 111 | 0,02 | 0,02 | 142 | 0,01 | 0,02 | 143 | 0,00 | 0,01 | 274 |
| ZnO | 45,21 | 13,54 | 29,94 | 62,02 | 4,10 | 7 | 57,22 | 14,33 | 25 | 21,87 | 21,46 | 98 | 61,67 | 1,90 | 3 | 0,02 | 0,03 | 104 |
| BaO | 0,04 | 0,06 | 132,82 | 0,02 | 0,04 | 213 | 0,05 | 0,08 | 150 | 0,07 | 0,05 | 70 | 0,04 | 0,06 | 170 | 0,19 | 0,21 | 108 |
| CdO | 0,31 | 0,15 | 47,00 | 0,25 | 0,17 | 69 | 0,26 | 0,40 | 152 | 0,07 | 0,06 | 91 | 0,18 | 0,26 | 144 | 0,03 | 0,05 | 198 |
| PbO | 0,45 | 0,27 | 58,85 | 0,11 | 0,13 | 124 | 0,57 | 0,46 | 81 | 1,01 | 0,65 | 65 | 0,47 | 0,40 | 86 | 78,76 | 3,97 | 5 |
| FeO | 9,28 | 9,18 | 98,93 | 0,32 | 0,35 | 109 | 0,43 | 0,51 | 120 | 22,12 | 17,57 | 79 | 0,04 | 0,08 | 232 | 0,01 | 0,02 | 169 |
| MnO | 0,05 | 0,06 | 121,90 | 0,02 | 0,03 | 140 | 0,03 | 0,03 | 123 | 0,04 | 0,04 | 101 | 0,03 | 0,04 | 115 | 0,02 | 0,05 | 239 |
| CuO | 0,02 | 0,04 | 219,64 | 0,02 | 0,05 | 226 | 0,02 | 0,03 | 153 | 0,01 | 0,01 | 173 | 0,01 | 0,03 | 320 | 0,11 | 0,19 | 172 |
| $CO_2$ | 31,31 | 2,49 | 7,95 | 34,67 | 1,83 | 5 | 31,76 | 7,92 | 25 | 25,72 | 7,69 | 30 | 34,25 | 1,05 | 3 | 15,75 | 0,73 | 5 |
| Total | 87,62 | 7,74 | 8,83 | 98,25 | 5,23 | 5 | 90,68 | 22,61 | 25 | 71,02 | 21,57 | 30 | 97,57 | 2,84 | 3 | 95,04 | 4,55 | 5 |
| | Average cations per formula unit | | | | | | | | | | | | | | | | | |
| Ca | 0,02 | | | 0,01 | | | 0,02 | | | | | | 0,04 | | | | | |
| Sr | | | | | | | 0,02 | | | | | | | | | 0,01 | | |
| Mg | 0,04 | | | 0,03 | | | 0,01 | | | | | | | | | | | |
| Zn | 1,54 | | | 1,93 | | | 1,88 | | | 0,95 | | | 1,95 | | | | | |
| Ba | | | | | | | 0,02 | | | | | | | | | 0,01 | | |
| Cd | 0,01 | | | 0,01 | | | 0,01 | | | | | | | | | | | |
| Pb | 0,01 | | | | | | 0,01 | | | 0,02 | | | 0,01 | | | 1,97 | | |
| Fe | 0,39 | | | 0,01 | | | 0,02 | | | 1,02 | | | | | | | | |
| Mn | | | | | | | | | | | | | | | | | | |
| Cu | | | | | | | 0,02 | | | | | | | | | 0,01 | | |
| Sum | 2,00 | | | 2,00 | | | 2,00 | | | 2,00 | | | 2,00 | | | 2,00 | | |